Master's thesis

NTNU
Norwegian University of Science and Technology
Faculty of Engineering
Department of Marine Technology

Stina Bjørgo Fimreite

Fluid Structure Interaction Analysis of Abnormal Wave Slamming Events

Master's thesis in Marine technology
Supervisor: Associate Prof. Zhaolong Yu
Co-supervisor: Prof. Jørgen Amdahl
July 2022

NTNU
Norwegian University of
Science and Technology

Stina Bjørgo Fimreite

Fluid Structure Interaction Analysis of Abnormal Wave Slamming Events

Master's thesis in Marine technology
Supervisor: Associate Prof. Zhaolong Yu
Co-supervisor: Prof. Jørgen Amdahl
July 2022

Norwegian University of Science and Technology
Faculty of Engineering
Department of Marine Technology

NTNU
Norwegian University of
Science and Technology

NTNU
Norges teknisk-naturvitenskapelige universitet
Institutt for marin teknikk

MASTER THESIS 2022

For

Stina Bjørgo Fimreite

Fluid Structure Interaction Analysis of Abnormal Wave Slamming Events

Koplet væske-konstruksjonsresponsanalyse av abnormale bølgeslagshendelser

Background:

Wind power is at the forefront of the green transition from classical fossil fuel to clean and decarbonizing energy. DNV report (DNV-GL, 2020) predicts that the installed floating wind capacity will have grown from 100 MW today to over 250 GW by 2050 – more than 20% of the offshore wind market, and the rest is taken by bottom fixed turbines with a capacity of 800-1000 GW by 2050. This represents huge market and great growth potential for offshore wind power.

Impact loads from steep and energetic waves is a critical design parameter for ocean structures. The tragic incident on the mobile drilling rig COSL Innovator at the end of 2015 proved this point to the ultimate degree. A steep wave impacted the deck-box of a mobile drilling rig, blew out windows and flooded parts of the living quarter. One person died and four were injured. Following the accident, the current industry practises for calculating air gaps and slamming loads on deck box in the case of negative air gap have been put under review. Simple design guidelines OGT 13 and 14 have been developed as a first approach to address and reflect the severity of wave impacts. Offshore wind turbines moving into exposed waters must design their structures to withstand steep and energetic waves as well.

Impact loads on the columns from breaking, or near breaking waves are significant and may become considerably higher than what is indicated in the relevant rules and regulations. The loads are characterized by short durations, large spatial variations, and high values, which put the measurement system in model tests at a considerable stress. Traditionally, ULS design is often adopted for the design against slamming, where the structure shall resist the design slamming pressure with minor damage. However, when more violent water slamming occurs in extreme or abnormal events, large structural stresses may occur that exceed the material yield stress, causing large plastic flow and permanent damage. The elastoplastic or fully plastic response of the structure will be strongly coupled with the hydrodynamic pressure, termed as hydro-elastoplasticity and hydro-plasticity. From the literature, coupling effects between structural response and hydrodynamic pressure during water slamming is generally limited to the hydroelastic effect. Little information can be found on the effect of hydro-elastoplastic or hydro-plastic slamming. When structural damage is concerned in extreme slamming, an uncoupled approach is often adopted by assuming a certain pressure profile, which is to be applied on the structure for the response. It is also unclear whether an artificial added mass should be added to the structure and, if so, the associated values to use.

Currently, the fluid structure interaction mechanism during water slamming is in general well developed in the elastic regime. However, when large plastic deformation comes into play, the interaction mechanism becomes unclear and significant knowledge gaps exist. Recent works by Yu et al. (2019) and Abrahamsen et al. (2020) with hydro-plastic models are promising tools to address the challenging interaction effects. The purpose of the master thesis is to investigate further fluid structure interaction effects of floater columns of a semi-submersible floating offshore wind turbine in extreme wave impacts. The first task is to reproduce existing drops tests with plastic damage using FSI modelling in LS-DYNA or ABAQUS so to verify the capabilities of FSI simulation approaches and to verify the numerical settings. The second task is to assess slamming damage of columns of the Odfjell floating offshore wind turbine with ALE simulations and analytical methods.

More specifically, the project work is proposed carried out in the following steps:

1. Perform a literature study of work and relevant code requirements (e.g. DNVGL-OTG –14, ABS rules) related to slamming on vertical faces on floating structures in order to establish a good understanding of past and current “state-of-the-art” methodologies for analytical and numerical assessment of loads and structural load effects.

2. Review of methods for analysis of dynamic, elastic-plastic response of unstiffened and stiffened plates subjected transient, dynamic loads, such as slamming loads, explosions, etc. Reference is made to Jones (1973), a twin paper by Yu et al. (2019) for hydro-plastic slamming theory and previous master theses by Anni Cao (2020), Louise Rolland (2018), Erik Skjeggedal (2017), Cyril Anglade (2017) og Marit Muren (2016).

3. Brief review of principles behind fluid structrue interanction (FSI) analysis of slamming loads with LS-DYNA ALE method or equivalent ABAQUS FSI simulation approaches. Conduct numerical simulations of drop tests of unstiffened plates by SINTEF OCEAN in the SLADE project. The goal is to verify capabilities of the FSI simulation approaches to reproduce the tests and to verify the numerical settings.

4. Using the verified numerical approach from pt. 3, perform ALE simulations of water

impact of a floating wind turbine foundation column. Focus shall be on structural response and residual strength.

5. Compare structural response from simulated drop test with response from design pressure impulse from DNV OTG-14.
6. Simulate rigid structure water impact with the model in pt. 4 for verification against analytical models. Key results will be pressure time history, spatial distribution, and impulses.
7. Analyse and discuss the results. Make conclusions and recommendations for further work in the master thesis project

Literature studies of specific topics relevant to the thesis work may be included.

The work scope may prove to be larger than initially anticipated. Subject to approval from the supervisor, topics may be deleted from the list above or reduced in extent.

In the thesis the candidate shall present his personal contribution to the resolution of problems within the scope of the thesis work.

Theories and conclusions should be based on mathematical derivations and/or logic reasoning identifying the various steps in the deduction.

The candidate should utilise the existing possibilities for obtaining relevant literature.

The thesis should be organised in a rational manner to give a clear exposition of results, assessments, and conclusions. The text should be brief and to the point, with a clear language. Telegraphic language should be avoided.

The thesis shall contain the following elements: A text defining the scope, preface, list of contents, summary, main body of thesis, conclusions with recommendations for further work, list of symbols and acronyms, references and (optional) appendices. All figures, tables and equations shall be numerated.

The supervisor may require that the candidate, in an early stage of the work, presents a written plan for the completion of the work. The plan should include a budget for the use of computer and laboratory resources, which will be charged to the department. Overruns shall be reported to the supervisor.

The original contribution of the candidate and material taken from other sources shall be clearly defined. Work from other sources shall be properly referenced using an acknowledged referencing system.

The report shall be submitted in two copies:
- Signed by the candidate
- The text defining the scope included
- In bound volume(s)

- Drawings and/or computer prints which cannot be bound should be organised in a separate folder.

Supervisors:
Associate Prof. Zhaolong Yu,
Prof. Jørgen Amdahl

Deadline: July, 31 2022

Trondheim, January 6, 2022

Abstact

During extreme sea conditions, slamming impact from large waves may cause significant damage to marine structures. Wave slamming induces high pressures with large spatial and temporal variations on the structure. During the impact, coupling between the hydrodynamic loads and structural response is important, and leads to a complex non-linear problem. While analytical models for describing both elastic and elasto-plastic response of the structures exist, these are idealised. Experimental and numerical assessments of wave impact are therefore necessary for sufficient understanding of the phenomenon.

Experimental drop tests of an unstiffened plate into still water were performed in the SINTEF Ocean project SLADE KNP to simulate wave impact. Plate impact with deadrise angles 0° and 4° were studied. These experiments have been numerically modeled using an ALE method in LS-DYNA and simulated. The numerical simulations found good accuracy between numerically and experimentally measured deformations of the impacting plate, verifying the modeling technique.

Further, slamming impact of a cylindrical floating wind turbine foundation column has been studied trough numerically simulated drop tests. A rigid model was simulated for comparison against theory, finding good accordance in pressure impulse acting on the structure. During deformable impact simulations of the column, significant permanent damage was caused to the structure. Residual stresses in the range of yield stress were also found, which are expected to decrease capacity in the damaged condition. Limiting cases for the physical representation are presented, giving limits for structural response.

Design pressures according to DNV OTG-14 were also applied to the cylindrical column, causing elastic vibrations and no permanent deformations. Compared to relevant drop simulations, the pressure impulse method is found to severely underestimate the structural response, providing unconservative results. This illustrates a need for further studies into design principles against slamming impact.

Sammendrag

I ekstreme sjøtilstandar kan bølgeslag påføre marine konstruksjonar store deformasjonar. Bølgeslag påfører konstruksjonen høge trykk med store variasjonar i tid og stad. Samankoplinga mellom hydrodynamiske laster og strukturell respons påverkar begge element, noko som fører til eit komplekst ikkje-lineært problem. Det finst analytiske modellar som beskriv både den elastiske og elasto-plastiske responsen til konstruksjonar, men desse er idealiserte. For ei fullstendig forståing av fenomenet er det derfor viktig med både eksperimentelle og numeriske studiar av bølgeslag.

Gjennom SINTEF Ocean prosjektet SLADE KNP ble det gjennomført eksperimentelle fall-testar av ei ustiva plate i stillestående vatn som ei idealisering av bølgeslag. Plata vart sleppt med vinkel 0° og 4° mellom plate og vassoverflate. Disse eksperimenta har blitt modellert numerisk i LS-DYNA ved hjelp av ein ALE-metode. Deformasjonane til plata målt frå eksperimenta og dei numeriske simuleringane samsvarte godt. Dette verifiserte den numeriske modelleringsteknikken.

Vidare vart bølgeslag mot ei sylindrisk flytande vindturbinfundamentsøyle analysert ved hjelp av numerisk simulerte fall-testar. Ein ikkje-deformerbar modell vart simulert som samanlikning med teori, noko som gav godt samsvar for trykkimpuls påført konstruksjonen under prosessen. Simuleringar av ei deformerbar søyle gav store permanente deformasjonar og spenningskonsentrasjonar med størrelse nær flytspenning. Det er forventa at dette gir redusert kapasitet i den skada tilstanden. Grensetilfelle for den fysiske representasjonen av bølgeslaget er presentert, noko som gir avgrensingar for responsen til konstruksjonen.

Designtrykk frå DNV OTG-14 blei også påført søyla. Dette gav elastiske vibrasjonar og ingen permanente deformasjonar. Samalikna med relevante fall-simuleringar undervurderer denne metoden deformasjonane til konstruksjonen, noko som gir ikkje-konservative resultat. Dette illustrerer behovet for vidare studiar av designmetodar som tek høgde for bølgeslag.

Preface

The work presented in this thesis is a Master's thesis at the department of Marine technology at the Norwegian University of Science and Technology (NTNU). This is the final part of a MSc degree with a specialisation in Marine Structures. The work is a culmination of five years of studies, and was performed during the spring semester of 2022.

The first part of the thesis work was suggested by the supervisors at NTNU. A great deal of time was spent getting familiar with numerical modeling techniques in both ABAQUS and LS-DYNA, the latter of which was chosen as the best suited approach. Midway through the semester, the second part of the thesis was changed after suggestions from Odfjell Oceanwind. This introduced a study of water impact of a cylindrical column using a verified modeling technique.

Although the work is performed with a specialisation in Marine structures, the topic of slamming requires structural assessments to be combined with hydrodynamic principles in order to give a full description. It has been both challenging and rewarding to implement topics presented in previous courses during the studies as well as acquiring new knowledge and skills.

Trondheim, 11th July 2022

Stina Bjørgo Fimreite

Acknowledgment

Firstly, I would like to thank my supervisor Associate Professor Zhaolong Yu for excellent guidance during the semester. The modeling guidance and help in running simulations have been essential for the thesis and are greatly appreciated.

I would also like to thank my co-supervisor Professor Jørgen Amdahl for valuable discussions and suggestions during guidance meetings. The new direction of the thesis suggested half-way through the semester also gave me a fresh input of motivation.

Furthermore, I would like to thank Bjørn Christian Abrahamsen and Øyvind Hellan for a very interesting meeting, giving me insight to the SINTEF Ocean SLADE project.

Finally, I would like to thank my friends at our office for motivation, humour and care when the work has been particularly challenging.

Contents

List of Tables

List of Figures

Nomenclature

Abbreviations

2D, 3D	Two/three dimensional
ALE	Accidental limit state
ALE	Arbitraty Lagrangian Eulerian
B.C.	Boundary condition
CFD	Computational Fluid Dynamics
DIC	Digital Image Correlation
EOS	Equation of state
FEM	Finite element method
FLS	Fatigue limit state
FSI	Fluid-structure interaction
OTG	Offshore Technical Guidance
RP	Recommended Practice
SDOF	Single degree-of-freedom
SLS	Serviceability limit state
ULS	Ultimate limit state

Greek symbols

β	Deadrise angle
Δt_{cr}	Critical time step

$\dot{\varepsilon}^*$	Normalised effective strain rate
η_b	Body shape function
γ_0	Material parameter in Gruneisen EOS
μ	Ratio between water entry velocity and change rate of wetted surface
ν	Poisson's ratio
ω_n	Wet natural frequency of beam
ϕ	Potential flow function
ρ	Density
σ_0	Initial yield stress
σ_y	Yield stress
ε, ε^p	Strain, plastic strain
ξ	Damping ratio

Latin symbols

$\overline{f}$	Generalised load
A	Johnson-Cook material parameter, σ_0
a	Nodal accelerations
A_p	Area of the plate flange of a stiffened panel cross section
$A_s = A_w + A_t$	Area of the stiffener cross section including web and top flange
A_t	Area of the top flange of a stiffened panel cross section
A_w	Area of the web of a stiffened panel cross section
A_{11}	Generalised added mass of beam
B	Johnson-Cook material parameter
b	Beam width
C	Strain rate sensitivity parameter
c	Speed of sound
$c(t)$	Instantaneous wetted length of the structure
C_i, i=0,1,..,6	Material parameter in linear polynomial EOS
C_p	Pressure coefficient
C_{11}, $\overline{k}$	Generalised stiffness of beam
E	Young's modulus

E_0	Initial internal energy
EI	Bending stiffness
h	Beam height
I	Impulse
K	Power law hardening material parameter
k_s	Penalty coupling stiffness
k_i, *i*=1,2,3	Linearised stiffness
L	Length of beam
M_0	Fully plastic bending moment
M_B	Mass per unit length
M_{11}, $\overline{m}$	Generalised mass of beam
m_{eq}	Eqivalent mass
n	Johnson-Cook/Power law hardening material parameter
p	Strain rate sensitivity parameter
p (p_a)	Pressure (atmospheric pressure)
p_1	First natural vibration frequency of beam
R	Radius of cylinder
$R(w)$	Force-deformation relationship
S_i, *i*=1,2,3	Material parameter in Gruneisen EOS
T	Natural period of vibration of structure
t	Time
t_d	Load duration
u	Nodal displacements
V	Water entry velocity
v	Nodal velocities
V_m	Deformation velocity of middle section of beam during plastic deformations
w	Vertical deflection
w_{max}	Maximum deflection
X	Position of plastic hinge relative to beam end
x	Spacial position on body
y(t)	Deflection amplitude

Chapter 1

Introduction

1.1 Background

On December 30th, 2016, the mobile semi-submersible drilling rig COSL Innovator was struck by a steep wave. The wave impact crushed several windows, causing water entry, killing one person and injuring four more. There was also permanent deformation caused to the deck box [8]. This accident has raised interest in the topic of slamming.

Slamming is a highly non-linear problem, characterized by high pressures, short durations and large spacial variations. The impacts cause significant structural response, which will interact with the wave forces, a phenomena denoted fluid-structure interaction. The interaction of the hydrodynamic force and elastic structural vibration, a field called hydro elasticity, has been extensively studied. Studies do however show that slamming impact also causes significant plastic deformations, calling for studies of hydroplasticity as well.

The coupling of the hydrodynamic force with plastic deformations leads to a non-linear problem. The response may be studied with experimental tests, numerical analysis or simplified methods, all with varying levels of accuracy. As experimental tests are expensive and time consuming, numerical simulations may be a good approach to further study the phenomenon. Some experimental tests are nevertheless necessary to validate the results of the numerical analyses. Simplified

methods are less accurate, but may be valid in initial stages of design.

The European Union has agreed to a joint reduction in greenhouse gas emissions of 55% by 2030, relative to 1990 emissions. Development of renewable energy technology plays an important role in reaching these goals. A promising field is offshore wind parks. Developing floating wind parks allows for moving the wind parks further offshore, utilising the ideal wind conditions. While wind conditions are more severe in exposed waters, this also exposes the structures to more significant wave loads. Wave slamming impact is therefore an important factor to consider in design of floating offshore wind turbines.

1.2 Objectives

1. Perform a literature study of work and relevant code requirements related to slamming on vertical faces on floating structures in order to establish a good understanding of past and current "state-of-the-art" methodologies for analytical and numerical assessment of loads and structural load effects.

2. Review of methods for analysis of dynamic, elastic-plastic response of unstiffened and stiffened plates subjected transient, dynamic loads, such as slamming loads, explosions, etc. Brief review of principles behind fluid structure interaction (FSI) analysis of slamming loads with LS-DYNA ALE method or equivalent ABAQUS FSI simulation approaches.

3. Conduct numerical simulations of drop tests of unstiffened plates by SINTEF OCEAN in the SLADE project. The goal is to verify capabilities of the FSI simulation approaches to reproduce the tests and to verify the numerical settings.

4. Using the verified numerical approach from pt. 3, perform numerical simulations of water impact of a floating wind turbine foundation column. Focus shall be on structural response and residual strength.

5. Compare structural response from simulated drop test with response from design pressure impulse from DNV OTG-14.

6. Simulate rigid structure water impact with the model in pt. 4 for verification against analytical models. Key results will be pressure time history, spacial distribution and impulses.

1.3 Scope

The overall goal of the thesis is to gain an understanding into the fluid-structure interactions (FSI) between hydrodynamic loads and structural response during wave impact, in particular elasto-plastic structural response. Furthermore, the accuracy of design loading from DNV OTG-14 shall be assessed. The work presented may be split in two main parts.

Firstly, the FSI modeling capabilities of numerical solvers will be explored. Using one of these methods, experimental drop tests of unstiffened panels undergoing plastic deformations will be modeled. The results from the numerical simulations will be compared against the experimental measurements for verification of the modeling technique.

Extreme wave impacts on a cylindrical wind turbine foundation will be studied. The wave impact is idealised as a drop of the structure into still water, modeled and simulated numerically. The results of the simulations will be analysed and verified against theory as far as possible. Finally, design practises for such offshore structures will be studied. The design practises will be compared with relevant numerical simulations of water entry events and evaluated.

1.4 Limitations

Early in the semester, FSI modeling of the experimental plate drop was attempted using the numerical solver Abaqus. After spending some time with this approach, preliminary results were not found to be satisfactory, so the technique was abandoned, instead using the FEM software LS-DYNA. In addition to the experimental drop tests of unstiffened panels in the SLADE KNP project, stiffened panel drop tests by Mori were also intended to be studied. Due to time constraints moving into the second part of the thesis, modeling of the stiffened panel drop tests were abandoned in agreement with my supervisor.

Running the numerical simulations was found to be time consuming due to slow file systems in the *Fram* supercomputer. Verifying the modeling of the column also proved to be challenging. Although not specified in the objectives, the study of the cylindrical column was intended to include a residual strength analysis in the damaged condition if time allowed. The option of modeling breaking wave impact on the cylinder in addition to the still water drop simulation was also discussed with the supervisors. However, both these studies were left for further work due to time contraints.

1.5 Literature review

The concept of slamming was first studied and described by von Karman in 1929 [9]. He studied the vertical water entry of rigid wedges, and formulated an analytical model describing the impact pressure by use of a flat plate approach. von Karman theory does however neglect the uprising of the water. This was corrected by Wagner in 1932 [10], who developed an analytical model of the water entry problem describing the uprising well.

The analytical model described by Wagner has been thoroughly studied and reworked in later years. Zhao and Faltinsen [11] studied water entry of rigid wedges with deadrise angles ranging from 4 to 81° using a numerical method. Greenhow and Yanbou [3], Cointe and Armand [12] and Korobkin [13] all studied different approaches to extend Wagner theory to apply for a rigid cylinder.

The concept of hydroelasticity was introduced in the 1990s and has been extensively studied since. Aarsnes [14] and Faltinsen, Kvålsvold, and Aarsnes [15] performed early experimental studies of the effect of the interaction between elastic structural response and hydrodynamic forces. Kvålsvold and Faltinsen [16] and Faltinsen [17] presented analytical models describing the interaction, with good correspondence to experimental results.

Faltinsen [17] used elastic beam theory and suggested splitting the slamming process in two stages: the structural inertia phase and the free vibration phase. During the structural inertia phase, the boundary value problem and the structural response may be solved simultaneously assuming no deflections of the structure due to the short period. The velocity of the structure at the end of the structural inertia phase

may be considered as initial velocity for the free vibration phase. Structural response is found by solving the initial value problem and pressures are found as pressures on a structure during harmonic oscillations.

In the process of understanding slamming, experimental tests have been important. Experiments by Aarsnes [14] and Faltinsen, Kvålsvold and Aarsnes [15] have previously been mentioned. Mori [18] performed drop tests of stiffened panels, documenting pressures and deflections. Abrahamsen et. al.[19] performed drop tests of unstiffened plates in conjunction with the SINTEF project SLADE KNP. In both studies, the s. These studies therefore provide interesting insight into hydroplasticity, i.e. the interaction between hydrodynamic loading and plastic deformations.

Abrahamsen et. al. [19] also presented an analytical hydroplastic model for comparison with experimental results, based on the hydroelastic model presented in Faltinsen [17]. The deflections of the plate during the free vibration phase are calculated based on the rigid plastic theory proposed in Jones [20]. The model assumes a perfectly plastic material and a deformation mode shaped as a pyramid. The suggested analytical model adequately predicts the deflections of the plate.

A recent development in the field of hydroplasticity is the twin papers from Yu et. al. [21],[22]. An analytical method approximating a plate as a beam is presented in the first paper. The travelling plastic hinge concept previously described by Jones [23] is applied. The structural response is split into three stages. During the first stage, a plastic hinge is created somewhere between the edge and the middle of the beam, and the hinge travels toward the center of the beam. During the second stage, the plastic hinge stays stationary at the center of the beam, and the velocity of the beam middle decreases. The beam becomes fully occupied by membrane stresses during the third stage. Permanent deflections is found when the beam middle velocity decreases to zero. The second paper verifies the model against numerical simulations, finding good correspondence in the results from the two methods.

Due to experimental tests being both time consuming and costly, numerical simulations are a good option. When using a well verified numerical method, simulations may give an accurate representation of the fluid-structure interaction even in the case of plastic deformations. In the more recent years, several relevant numerical

studies have been performed.

Truong et. al. [2] modeled impact of stiffened plates and validated the numerical models against experimental results. Cheon et. al. [24] performed parametric studies, studying the effect penalty factor, mesh, impact velocity, structural flexibility, stiffener size and entrapped air cushions on the pressure distribution. Stenius et. al. [25] studied the effect of parameters such as impact velocity, deadrise angle and boundary conditions of stiffened panels thorugh numerical simulations. Truong et. al. [26] performed a benchmark study, comparing several different numerical fluid-structure interaction solvers.

1.5.1 Previous Work

The effect of hydroelasticity and -plasticity has been studied in several Master theses at the department of Marine technology previously. As summary of the work and most important findings is listed below.

Muren [27] studied the possibility of using pressure impulses from rigid model tests to include effects of hydroelasticity and added mass by modification of the impulse. Parametric studies found great significance of both contributions, leading to very conservative results if they are neglected.

Anglade [28] performed a comparison of a slamming analysis including FSI and not including FSI, meaning pressures are calculated for an assumed rigid structure and then applied to the structure. The study found a reduction in pressures and response but longer loading period for the column experiencing FSI. An inclined analysis simulating wave impact also illustrated the localization of the damage, as no global effects were found.

Skjeggedal [29] studied wave impact responses of semi-submersibles. Numerical simulations of drop tests were firstly verified against experimental drop tests reported in Faltinsen [30]. Drop tests were simulated for rigid, elastic and elasto-plastic stiffened panels, as well as a full scale semi-submersible column. The structural responses were compared with the response due to DNV OTG-14 pressure loads, finding good correspondence. The responses were also estimated using simplified single degree of freedom systems, which were found to give conservative estimations.

Rolland [1] analysed the experimental drop tests performed in the SINTEF Ocean SLADE KNP project, also presented in Abrahamsen et. al. [19], with numerical simulations using LS-Dyna. A stiffened panel drop test was also simulated and compared with the SDOF simplified method presented in DNV RP-C204, which was found to underestimate the total response of the structure. The simplified method was nevertheless found helpful in initial design process.

Cao [31] modeled local water impact of a steel column of a typical semi-submersible platform, as well as drop tests of the column. Parametric studies were performed to see the effect of material, plate thickness and drop velocity. Calculations from simplified, namely fourth order Runge-Kutta and SDOF analogy both underestimated the maximum elastic deformations. An attempt to apply the pressure output of the deformable model to the underformed model was also attempted, but this was determined to be an unsuitable approach.

Kingell [32] studied the breaking wave phenomenon through numerical FSI simulations in LS-Dyna. A stiffened panel impacted by a breaking was modeled. Parametric studies were performed to determine the effect of the size of the impacting water domain and effect of air entrapment. Including coupling to air in the simulations caused a somewhat reduced permanent deflection and lower peak pressures. The analytical model suggested by Yu et. al. [21] somewhat overestimated the deflections, but produced a good fit for the pressure history at the center of the panel.

1.5.2 Rules and regulations

Following the COSL Innovator accident, DNV introduced offshore technical guidance 13 and 14. Both documents are based on ULS, giving design guidance based on 100 year return periods of environmental actions. DNV OTG-13 [33] gives instructions for calculating air gap of column stabilised offshore units. Calculations are based on metocean conditions and statistical modeling.

DNV OTG-14 [7] deals with wave impact loads on column stabilized units experiencing negative air gap. Instructions are given for creating design pressures which should be applied to 3 x 3 m^2 and 6 x 6 m^2 panels on the structure. Peak values of the design pressure may be found based on the vertical position of the panel relative to the 100 year upwell level. Based on peak pressure, sustained pressures may

be found as fractions of the peak value. The maximum peak pressure to be used is 1.3 MPa. Design pressures have been calibrated excluding hydroelastic effects.

DNV recommended practice C204 [4] gives recommendations for design against accidental loads, including explosions. Explosions are defined with large temporal and spacial pressure variations, characteristics also shared by slamming impact. Design practice against explosions is therefore also applicable in considerations of slamming. DNV RP-C204 describes a simplified approach to estimating the structural response due to explosion pressures by use of a single degree of freedom analogy. Using Biggs method, the structural response may be found from diagrams based on load history, resistance curves and load duration relative to system natural frequency.

1.6 Structure of the thesis

The following part of the thesis is divided in 7 more chapters. The contents of each chapter is presented below.

Chapter 2: Relevant background theory on slamming, structural response and finite element analysis is presented.

Chapter 3: Experimental drop tests of an unstiffened plate are recreated through numerical modeling. Focus is given to the structural response of the plate.

Chapter 4: The numerical approach from Chapter 3 is used for modeling a drop test of a rigid cylinder. The pressures measured on the cylinder during the drop is compared with relevant theory.

Chapter 5: A drop test of a deformable cylinder is simulated numerically, using the same model as in Chapter 4. Deformations of the cylinder due to the impact are studied and discussed.

Chapter 6: Pressure impulses are applied to the cylinder discussed in the previous chapter. Deformations are measured and compared with deformations from the drop test.

Chapter 7: Discussion of results and approach.

Chapter 8: Conclusions and recommendations for further work.

Chapter 2

Theory

2.1 Slamming

As mentioned in the introduction, slamming is a highly non-linear phenomenon, causing pressures with large variations in space and time on the affected structure.

An early model for calculating slamming pressures on an impacting rigid body was presented by Wagner in 1932 [10]. The model assumes small deadrise angles between the body and the water. This model separates the water into a inner domain, outer domain and jet domain. The jet domain represents the water spray at the intersection between structure and fluid free surface, while the inner domain represents the fluid at the spray root. The outer domain is located outside and below the two aforementioned domains.

A simplified version of Wagners model is presented in Faltinsen [34] which focuses on the outer fluid domain. The problem can then be simplified to a 2D boundary value problem where the requirement of no flow through the body is transferred to a flat plate equivalent. The instantaneous length of the plate $c(t)$ represents the wetted surface of the structure. The resulting pressure and velocity potential on the body are given by Equations (2.1) and (2.2). Here, the water entry velocity is assumed to be constant, V, but the same terms may be found with a variable velocity $V(t)$.

$$p - p_a = -\rho \frac{\partial \phi}{\partial t} \tag{2.1}$$

$$\phi = -V\sqrt{c(t)^2 - x^2} \tag{2.2}$$

Combining the two equations, the pressure, given as a function of time and location on the structure, is expressed by Equation (2.3). The first term is related to the change rate of wetted surface and may therefore be taken as the slamming pressure, while the second term is related to the change in impact velocity. The second term is therefore called the added mass pressure. When the impact velocity is constant, the added mass term is zero and only the slamming pressure remains.

$$p - p_a = \rho V \frac{c(t)}{\sqrt{c(t)^2 - x^2}} \frac{dc}{dt}(t) + \rho \frac{dV}{dt}\sqrt{c(t)^2 - x^2} \tag{2.3}$$

The wetted surface may be found by solving Equation (2.4), where $(x, \eta_b(x))$ corresponds to the intersection between the body and the free surface. $\eta_b(x)$ is thus a function, describing the shape of the impacting body.

$$\eta_b(x) = \int_0^t \frac{V|x|}{\sqrt{x^2 - c(t)^2}} dt \tag{2.4}$$

Equation (2.4) is solved by introducing the term $\mu(c)$, where $\mu(c)$ is the ratio between the water entry velocity and the change rate of the wetted surface. The equation may then be rewritten as Equation (2.5).

$$\eta_b(x) = \int_0^x \frac{x\mu(c)}{\sqrt{x^2 - c^2}} dc \tag{2.5}$$

A simple way of estimating the wetted surface length $c(t)$ is to assume a linear dependence on c for $\mu(c)$, i.e. $\mu(c) = A_0 + A_1 c$. Further, the body equation η_b is assumed as a second order polynomial with no constant constant term. An example is a triangular wedge with deadrise angle β between the initial water line and the body, where $\eta_b = |x| \tan \beta$. The wetted surface length during water entry

of such a rigid wedge is given in Equtaion (2.6).

$$c(t) = \frac{\pi V t}{2 \tan \beta} \tag{2.6}$$

2.1.1 Predicted wetted surface of cylinder

Slamming pressures on a rigid cylinder is a complicated matter as the deadrise angle between the body and the water changes rapidly. The body equation for a cylinder is given as $\eta_b(x) = R - \sqrt{R^2 - x^2}$, R being the radius of the cylinder. Faltinsen [34] gives a solution method for the predicted wetted surface by approximating the body equation as a second order polynomial. This is not a suitable approximation for a cylinder, as the curvature of the cylinder is constant.

Greenhow and Yanbao [3] studied the water entry of a rigid cylinder. They also used a polynomial fit to describe the body equation, but included an infinite number of terms. $\mu(c)$ and $\frac{Vt}{R}$ are reported as infinite series, reproduced in Equations (2.7) and (2.8).

$$\mu(c) = \sum_{m=0}^{\infty} \frac{(2m+1)!!(2m-1)!!}{(2m+2)!!(2m)!!} \left(\frac{c}{R}\right)^{2m+1} \tag{2.7}$$

$$\frac{Vt}{R} = \sum_{m=0}^{\infty} \frac{(2m+1)!!(2m-1)!!}{(2m+2)!!(2m)!!(2m+2)} \left(\frac{c}{R}\right)^{2m+2} \tag{2.8}$$

The solutions to Equations (2.7) and (2.8) are calculated in MATLAB, with calculations explained in Appendix A. The summations of the series are illustrated in Figure 2.1 as functions of c/R. From this, $\frac{dc}{dt}(t)$ may be found as $V/\mu(c)$ so that the pressures may be calculated from Equation (2.3). The time instance related to each pressure curve can be found from Vt/R, as this relates to each wetted surface length c to a time instance t.

An initial assumption of the Wagner model for calculating pressures is small deadrise angles between the structure and fluid. This is obviously not satisfied for the outer part of a cylinder. Results given in Greenhow and Yanbao [3] show that the method presented in this section quite accurately predicts the wetted surface of the

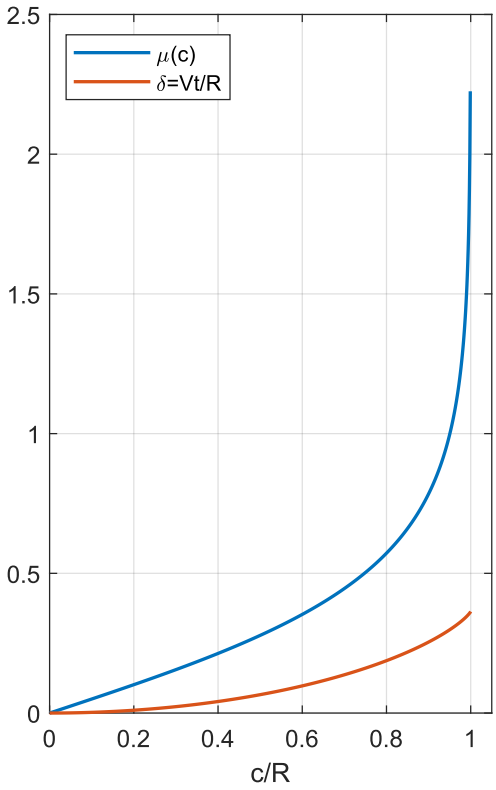

Figure 2.1: Solutions to Equation (2.7) and (2.8) of Wagner flat plate approach for cylinder, based on Greenhow and Yanbao [3].

cylinder when compared with experiments. The pressure distributions follow the same trend as the experimentally measured pressures, but somewhat overestimates the values. The method does not correspond well with experimentally measured forces acting on the body.

2.2 Structural Response Analysis

According to DNV RP-C204 [4], the structural response due to transient loading may be classified in three categories: the impulsive domain, the dynamic domain and the quasi-static domain. The relevant response domain is determined by the relation between the load duration t_d and the fundamental period of vibration of the affected region T. The response may be categorised as following:

$$\begin{array}{lccccc} \text{Impulsive domain:} & & & t_d/T & < & 0.3 \\ \text{Dynamic domain:} & 0.3 & < & t_d/T & < & 3 \\ \text{Quasi-static domain:} & 3 & < & t_d/T & & \end{array}$$

In the impulsive domain, the response depends on the load impulse, as defined in Equation (2.9). The maximum deformation of the structure w_{max} may be found by solving Equation (2.10) by iterations, where $R(w)$ is defined as the force-deformation relationship and m_{eq} as the equivalent mass of the affected component. In the quasi-static domain, the load duration is significantly longer than the fundamental vibration period of the component, which is uncommon with regards to slamming. The response may nevertheless be found directly or with iterations be equating the force-displacement relationship with the internal work at the end of the deformation. The third type of loading in the dynamic domain leads to the necessity of solving the dynamic equilibrium equations. In the case of slamming, this leads to a complex coupling between the structure and the hydrodynamic forces.

$$I = \int_0^{t_d} F(t)dt \tag{2.9}$$

$$I = \sqrt{2m_{eq} \int_0^{w_{max}} R(w)dw} \tag{2.10}$$

The pressures calculated by Wagner's model [10], presented in Section 2.1, assumes a rigid structure and may therefore not be used directly for calculating a structural response. Loading in the dynamic domain requires dynamic equilibrium between the structure and the hydrodynamic forces. In the case of an elastic structural response, the fluid-structure interaction is dubbed hydroelasticity, while the occurrence of elasto-plastic structural response leads to the necessity of hydro-

elastoplastic or hydro-plastic models. DNV RP-C205 [35] recommends that hydroelasticity should be considered when determining the structural response when the non-dimensional term in Equation (2.11) is less than 1/4.

$$\sqrt{\frac{EI}{\rho L^2}}\frac{\tan\beta}{|V|} < 0.25 \tag{2.11}$$

2.2.1 Hydroelasticity

A method for calculating the hydroelastic response of a structure was presented in Faltinsen [17]. The structure is represented by an Euler beam with corresponding bending stiffness EI and mass per unit length M_B. The problem is simplified to two dimensions, solving the equation of motion and boundary value problem simultaneously. The structural response is split in two stages: the structural inertia phase and the free vibration phase.

During the initial structural inertia phase, the beam is accelerated by the hydrodynamic force. However, due to the short time scale of this phase, no deflections are instigated. The accelerated structure therefore has an initial velocity into the free vibration phase, which when averaged over the length of the beam is equal to the impact velocity [34].

During the free vibration phase, the beam experiences elastic vibrations with an added mass and damping effect caused by the hydrodynamic pressure. Only the first mode shape of the vibration is considered, as higher mode shapes have lower amplitude and are faster damped.

A simplified approach to the free vibration phase problem is presented in Faltinsen [34]. By averaging the impermeability condition, requiring no flow through the body, over the length of the body, the problem simplifies to what is expressed Equation (2.12). The terms on the left side of the equation are the mass and stiffness terms, while the term on the right hand side represents the added mass. The equation may be solved for the deflection amplitude $y(t)$ by multiplying with the mode $\cos(p_1 x)$ and integrating over the length of the body. This results in the

simple eigenvalue problem in Equation (2.13).

$$M_B\ddot{y}_1(t)cos(p_1x) + EI \cdot p_1^4 y_1(t)\cos(p_1x) = -\rho\ddot{y}_1(t)\frac{2}{\pi}\sqrt{(L/2)^2 - x^2} \quad (2.12)$$

$$(M_{11} + A_{11})\frac{d^2y}{dt^2} + C_{11}y_1 = 0 \quad (2.13)$$

The deflections of the beam are then given by Equation (2.14), where w_n is the wet natural frequency of the beam and $p_1 = \frac{\pi}{L}$ for a beam which is hinged in both ends. The amplitude of oscillation C may be determined from the initial condition $\dot{w}|_{t=0} = V$ averaged over the length of the body. The spacial mode shape is one sinusoidal half-wave, with the temporal amplitude also varying in a sinusoidal manner.

$$w(x,t) = y_1(t)\cos p_1 x, \text{ where } y_1(t) = C\sin\omega_n t \quad (2.14)$$

2.2.2 Hydroplasticity

An analytical model for calculating the permanent deformations of a structure due to hydrodynamic and structural response interaction was presented in Yu et. al. [21]. The hydroplastic model also divides the structural response into a structural inertia phase where no deflections are instigated, and a free deflection phase where the body deforms with an initial deformation velocity equal to the impact velocity V. The hydroplastic model describes the deformations during the free deflection phase in three stages: stage 1 with travelling plastic hinges, stage 2 with stationary hinges and stage 3 with pure tension deformations. The beam representation from the hydroelastic model is also used here.

Some key assumptions are made in the model. The elastic energy is assumed small and negligible compared to the plastic strain energy. The material of the structure is assumed to be rigid-perfectly plastic, and strain rate and strain hardening effects are assumed negligible. Shear deformations are also assumed to be small and therefore neglected. Finally, deflections are assumed to be finite but small compared to the beam length.

At the beginning of the free deflection phase, the beam is undeformed. Plastic hinges are created between the beam ends and middle point, an initial distance

X(0) from the beam end. Deflections are symmetric about the midpoint, so only half the beam length is considered in further explanations. The central part of the beam has velocity equal to the impact velocity while the region closer to the end has a linearly increasing velocity towards the centre. During the first stage, the plastic hinges travel towards the centre of the beam. Stage 2 is instigated when the travelling hinges reach the center of the beam. The beam will then continue to deflect with the stationary hinge at the center, but the velocity of the midpoint will start decreasing. As the deflections continue to increase, bending moments decrease and membrane forces increase. When the cross-section if completely occupied by membrane forces, stage 3 is instigated. Permanent deformation is reached then the midpoint velocity has decreased to zero. The displacement and velocity fields during the different stages of deformation are illustrated in Figure 2.2.

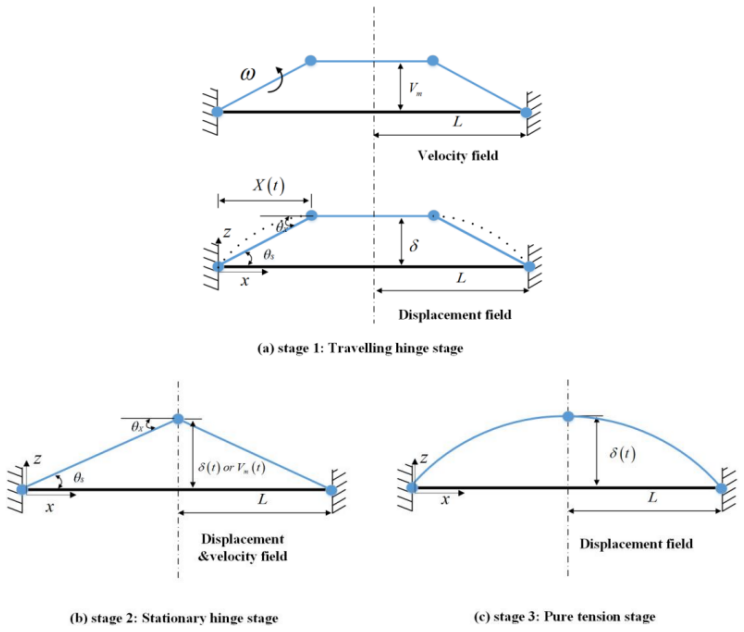

Figure 2.2: Displacement and velocity fields during the different stages of deformation, reproduced from Yu et. al. [21].

The hydrodynamics of the problem are solved as a 2D boundary value problem where the infinite frequency free-surface boundary condition is applied. The impermeability condition is only satisfied when averaged over the length of the body.

The resulting pressure, presented in Equation (2.15), has two contributions: the first term is an added-mass contribution due to the structural deformation mode while the second term is an added-mass contribution due to the change in deformation mode.

$$p = -\rho \dot{V}_m(t)\phi - \rho V_m(t)\frac{\partial \phi}{\partial t} \tag{2.15}$$

The hydroplastic model describes two paths that may be followed during the structural response. Structures following path 1 deform as previously described with travelling hinges during stage 1, stationary hinges during stage 2 and pure membrane action during stage 3. It may however happen that the cross-section becomes fully occupied by axial stresses before the travelling hinges reach the center of the beam. In this case, the structure jumps from stage 1 directly to stage 3, causing a sudden change in the midpoint velocity. This is defined as path 2. In some cases, the velocity may also decrease to zero during stage 2, in which case the structure follows path 1 but reaches permanent deflection during stage 2 and never reaches stage 3.

Plate strips from unstiffened plates are typically long and thin, causing path 2 to be a typical deformation pattern and stage 3 to be the main deformation stage. Stiffened panels usually have a higher capacity for bending. They therefore typically follow path 1, with stage 1 and 2 being more important than for plates. For high values of non-dimensional velocity, stiffened panels may also follow path 2.

Four non-dimensional parameters affecting the structural response, listed below, were identified by Yu et. al. ρ is the density of the structure, b, L and h are the width, length and height of the beam respectively, M_0 is the fully plastic bending moment and c_e is the sound of speed in water.

- Non-dimensional velocity $V_{nd} = V\sqrt{\frac{\rho L^3}{M_0 h/b}}$
- Non-dimensional mass $m_{nd} = m/\rho bL$
- Ratio of initial travelling hinge position relative to beam half length

$$X_{nd} = \frac{X(t=0)}{L} = \sqrt{\frac{24}{\left(V\sqrt{\frac{\rho L^3}{M_0 h/b}}\right)^2} \cdot \frac{VL}{c_e h}}$$

- Area ratios $A_{ps,nd} = A_p/A_s$ and $A_{wt,nd} = A_w/A_t$ (only for stiffened panels)

The permanent deflection of plates is most impacted by the non-dimensional velocity, with a seemingly linear relationship between non-dimensional velocity and permanent deflections. Stiffened panel deformations are also highly dependent on non-dimensional velocity, although the relationship with permanent deflections becomes non-linear. For stiffened panels, it is also possible to determine a limit non-dimensional velocity where the deformations will change from path 1 to path 2.

2.2.3 Single degree of freedom analogy

DNV RP-C204 [4] explains a simplified method for calculating the structural response to a load impulse, using a simple single degree of freedom (SDOF) system. The method is in the RP introduced in relation with structural design against explosions. Explosions are characterised by large spacial and temporal pressure distributions, a characterisation also shared by slamming impact. It is therefore also considered a good simplified approach for estimating the structural response due to slamming pressures. The method assumes that the structure may be approximated by a SDOF system, where the response due to a pressure impulse may be found from a Bigg's design chart.

The SDOF system analogy assumes that the system, when exposed to a dynamic pressure impulse, will deform in the same deformation mode as when exposed to static loading. The deformation mode is given in Equation (2.16), where the spacial shape function $\phi(x)$ is known and the displacement amplitude $y(t)$ will depend on the loading.

$$w(x,t) = \phi(x)y(t) \tag{2.16}$$

The equations of equilibrium of the original system may then be rewritten as in Equation (2.17). $\overline{m}$, $\overline{k}$ and $\overline{f}$ are the generalised mass, bending stiffness and load, respectively. These may be calculated for the system by integrating distributed contributions over the length and summarising concentrated contributions.

$$\overline{m}\ddot{y} + \overline{k}y = \overline{f}(t) \tag{2.17}$$

In order to use the SDOF system as an estimation for the structure, the maximum elastic capacity and deformation at the end of the elastic domain must be calculated. This may be calculated analytically or numerically when the generalised mass, stiffness and load are known. The natural period of the SDOF system must also be calculated, as given in Equation (2.18).

$$T = 2\pi\sqrt{\frac{\bar{m}}{\bar{k}}} \tag{2.18}$$

When the SDOF system is exposed to a triangular pressure impulse, the response of the structure is illustrated in Figure 2.3. The duration of the pressure impulse t_d relative to the natural period of the system and the maximum load relative to the elastic load capacity are two key parameters. The shape of the resistance curve, i.e. the load-deformation curve, is also necessary for estimating the response. The Bigg's chart for a triangular load impulse with rise time $0.5t_d$ is given in Figure 2.3, but Bigg's charts for load impulses with different rise times may also be found in DNV RP-C204 [4].

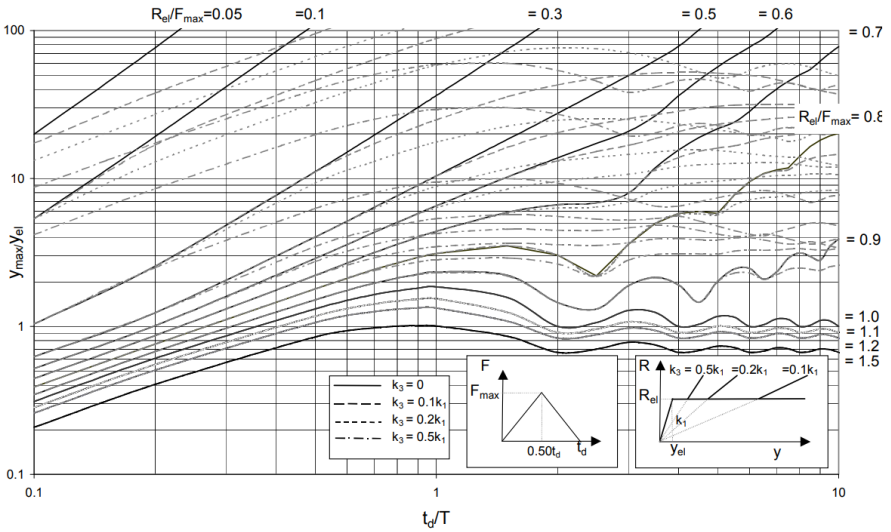

Figure 2.3: Bigg's design chart describing the dynamic response of a SDOF system due to a triangular pressure impulse with rise time $0.5t_d$, reproduced from DNV RP-C204 [4].

In order to apply this method for estimation of structural response, a resistance

curve for the structure must be known. The resistance curves used in the Bigg's chart are idealised, so typical resistance curves are not expected to fully satisfy the assumed shape. Resistance curves for the structure should therefore be linearised in three steps, a so-called tri-linearisation as is illustrated in Figure 2.4. The lighter curve in the figure represents the true resistance curve, while the darker curve represents the linearisation. The initial stiffness k_1 represents the elastic resistance, while following stiffnesses k_2 and k_3 represent the plastic resistance.

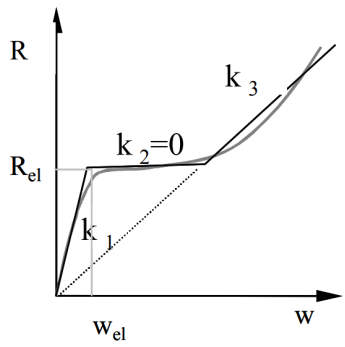

Figure 2.4: Tri-linearisation of a resistance curve, reproduced from DNV RP-C204 [4].

When a linearised curve has been fitted to the structural resistance curve, the elastic resistance R_{el} and the deflection at the end of the elastic domain w_{el} corresponds to the intersection between k_1 and k_2. The load impulse should then be idealised as a triangular load impulse, where F_{max} and t_d are known. The correct curve in the Biggs chart may then be identified based on relative load and the tri-linearisation of the resistance curve. Finally, the response may be found based on the duration of the load impulse.

2.3 Limit State Conditions

In structural design, it is important to consider a wide range of scenarios. Four limit states, determining resitance against different failure modes, are defined in NORSOK standards: ultimate limit state (ULS), accidental limit state (ALS), fatigue limit state (FLS) and serviceability limit state (SLS). Wave slamming loads are important to consider in ULS and ALS analyses and may be considered environmental actions [36].

ULS aims to ensure safety in operation considering expected loads on the structure. Structural integrity analysis must be performed for environmental loads with annual exceedance probability of 10^{-2}. Considering ULS, the structure shall be designed considering a load safety factor of 1.3 and a material safety factor of 1.15.

Accidental and unexpected loads are handled with the ALS. An important consideration is large environmental loads, so ALS requires design against environmental actions with annual exceedance probability of 10^{-4}. Safety factors in ALS are set to 1. ALS design checks also include a structural integrity analysis in the damaged condition, considering environmental actions with a 100 year return period.

2.4 Finite Element Analysis in LS-Dyna

LS-DYNA is a finite element program by Livermore Software Technology Corporation. It is a multi-physics solver, with modules for mechanical problems as well as fluid, thermal, electromagnetic and particle problems. The mechanical solver specialises in highly nonlinear, transient dynamic problems, solving by means of explicit or implicit time integration. This solver also allows for fluid-structure interaction trough the inclusion of an arbitrary Lagrangian Eulerian method [37].

2.4.1 Arbitrary Lagrangian Eulerian method

There exists two main methods of describing how materials move through space and time: Lagrangian and Eulerian. The Lagrangian description is often dubbed the material description, as this tracks the motion of every material element. This way of describing the physics is common in finite element analysis, where the displacements and velocities of mesh nodes are tracked. The Eulerian description is on the contrary dubbed the spacial description as the flow of the entire material is tracked. Using the Eulerian description, the mesh is kept stationary and the material is allowed to flow through it, with flow velocities being tracked. This approach is commonly applied in fluid dynamics problems [37].

A drawback of the Lagrangian formulation when applied to cases with significant deformations are mesh distortion, which will cause the finite element analysis to fail. The Eulerian formulation however requires a large stationary mesh to track the motion of the material and may have difficulties tracking thin material interfaces.

The solution to the problems presented is the Arbitrary Lagrangian Eulerian method, hereafter dubbed ALE. The ALE method combines the flow of material through a predefined mesh of the Eulerian formulation with the mesh motion of the Lagrangian formulation. This method has proven helpful in mechanical problems involving highly distorted structural problems and fluid modeling.

The ALE method is applied in LS-DYNA through three steps: mesh distortion, mesh smoothing and advection. During the mesh distortion step, a Lagrangian formulation is applied to the ALE mesh, tracking the motion of the mesh. The initially regular mesh then becomes distorted. During the second step, the mesh distortions are smoothed, again giving a regular mesh. Finally, during the advection step, material flows trough the ALE smoothed mesh to the same locations as at the end of the Lagrangian step.

Stability of the ALE method is ensured with the Courant-Friedrichs-Lewy condition, as expressed in Equation (2.19).

$$\Delta t_{cr} = \min \left[\frac{\Delta x^e}{c}, \frac{2\Delta x^e}{\nu^e} \right] \tag{2.19}$$

2.4.2 Coupling between ALE domain and Lagrangian structure

During slamming impact, the structure may be significantly damaged. The deformations are however still finite and rather moderate compared to the interruption of the fluid flow. The structure may therefore be modeled using a Lagrangian approach while an ALE approach is more useful for the fluid domain. This requires the necessity of interaction between the two types of domains.

Coupling between a Lagrangian and ALE domain is enabled if penetration occurs. Penetration is defined when the Lagrangian structure moves into the ALE mesh. A response is then applied to the both domains.

Several methods for ensuring coupling between the Lagrangian structure and the ALE material are implemented in LS-DYNA: among these ar the constraint-based method which requires that the velocities of the Lagrangian structure and ALE material are the same, and the penalty-based method which introduces spring forces on the coupling points. The recommended coupling method in most cases is the

penalty-based method [37].

As mentioned, the penalty-based coupling method introduces springs between the Lagrangian structure and the ALE material surface. As the structure moves into the ALE material, forces are applied to both surfaces. The spring forces will be linear with regards to the penetration depth, and may be scaled by the user. According to Truong et. al.[2], the coupling stiffness may be found from Equation (2.20) where K is the bulk modulus of the fluid, A is the Lagrangian structure element area and V is the volume of the fluid element being penetrated. f represents the user scale factor.

$$k_s = f\frac{KA^2}{V} \tag{2.20}$$

2.4.3 Explicit time integration

The explicit time integration in LS-DYNA is performed using an explicit central difference scheme [38]. Using an explicit integration method, the displacements at time *n+1* are a function of the displacements and forces at time *n*. The integration method used in LS-DYNA is explained in this section. Firstly, the accelerations are calculated at the present time step *n*.

$$a^n = M^{-1}(P^n - F^n + H^n) \tag{2.21}$$

M is the diagonal mass matrix, *P* is external and body forces, *F* is the stress divergence vector and *H* is the hourglass resistance. Velocities are calculated between time steps, at *n+1/2*, as illustrated in Equation 2.22.

$$v^{n+1/2} = v^{n-1/2} + a^n\Delta t^n, \qquad \Delta t^{n+1/2} = \frac{\Delta t^n + \Delta t^{n+1}}{2} \tag{2.22}$$

Finally the displacements are calculated from the velocities, given in the first part of Equation (2.23). The new geometry of the structure is found by adding the nodal displacements at time *n+1* to the initial body position x^0.

$$u^{n+1} = u^n + v^{n+1/2}\Delta t^{n+1/2}, \qquad x^{n+1} = x^0 + u^{n+1} \tag{2.23}$$

The stability condition of this integration scheme is given in Equation (2.24). ω_{max} is the larges natural frequency of the system and ξ is the damping ratio. For an undamped system, the final factor disappears.

$$\Delta t_{cr} \leq \frac{2}{\omega_{max}} \left(\sqrt{1 - \xi^2} - \xi \right) \tag{2.24}$$

2.4.4 Material

In elastic material behaviour, there is a linear relationship between loading and deformation. When elastic loading is reversed, the structure will resort back to the original configuration. Plastic material behaviour describes the material behaviour after the onset of initial yield. When unloading from loads in the plastic domain occurs, the structure will resort back in a path parallel to elastic unloading, but permanent deformations are created, as is illustrated by the stipled line in Figure 2.5(a).

Figure 2.5 illustrates two different elastoplastic material models. The elastic-perfectly plastic material illustrated in Figure 2.5(a) reaches ultimate loading at the onset of yield. Metals do however often have significant residual strength after initial yield is reached, as illustrated for an elastoplastic material model in Figure 2.5(b). This increase in yield stress due to plastic strains is called work-hardening. A non-linear material description is therefore necessary to model the material behaviour of metals.

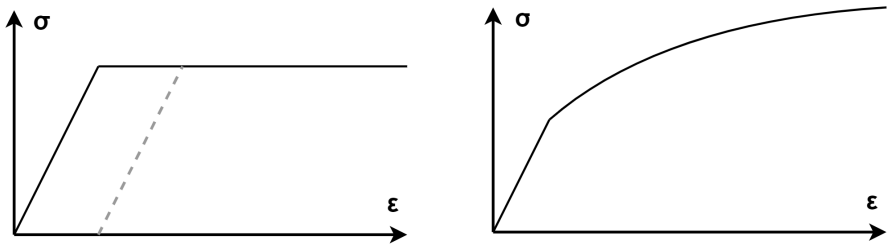

(a) Elastic-perfectly plastic material **(b)** Elastoplastic material

Figure 2.5: Material behavior of different elastoplastic materials.

An elasto-plastic material is described by three relations: initial yield condition, hardening rule and flow rule. The initial yield condition gives the initial limit for

material yield, i.e. the equivalent von Mises stress equal to σ_0. A hardening rule describes how the yield criterion is changed by the plastic flow history, i.e. how the two materials behave differently after initial yield in Figure 2.5. The hardening rule also describes the material response to reversed loading: kinematic hardening meaning that the reversed loading yield criteria is dependent on the original yield criterion and isotropic hardening meaning a symmetric yield criterion of reversed loading. The difference is illustrated in Figure 2.6. These two conditions form the consistency condition of the material. Finally, a flow rule is required to describe the relation between stress and strain increments, i.e. in the elastic domain $d\sigma = Ed\varepsilon$.

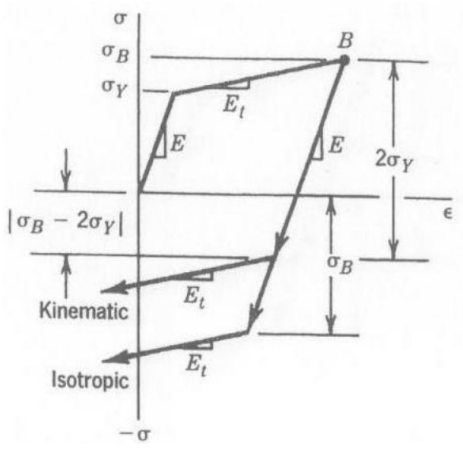

Figure 2.6: Illustration of kinematic and isotropic hardening rules, reproduced from Moan [5].

The plastic strains in the materials are not the only factor which may affect the yield stress: plastic strain rate usually also plays an important role for metals. This is particularly true during impacts, where the strain rate may become very high. Strain rate effects increase the yield stress, and a useful way of describing this effect is a modified form of the Norton creep law, see Equation (2.25). $R(\varepsilon^p)$ represents the plastic hardening, $\dot{\varepsilon}^*$ is the normalised plastic strain rate and C is a constant describing the strain rate sensitivity. σ_v is the viscous contribution to the yield stress [39].

$$\sigma_v = (\sigma_0 + R(\varepsilon^p)) \left[(1 + \dot{\varepsilon}^*)^C - 1\right] \tag{2.25}$$

The Johnson-Cook material model is a material model often applied for metallic materials. These materials are often strain rate dependent, with a rate dependence increasing and yield stress decreasing with temperature. The plastic hardening is described by a power law while the rate dependence is accounted for by a modified form of the Norton creep law [39]. A simplified version of the model is presented in Equation (2.26), neglecting temperature sensitivity. Here, A is the initial yield stress σ_0, B and n are plastic hardening parameters and C is a parameter relating to the strain rate sensitivity. ε^p is the plastic strain and $\dot{\varepsilon}^*$ is the normalized effective strain rate. This model is implemented in LS-DYNA as *MAT_098_SIMPLIFIED_JOHNSON_COOK.

$$\sigma_y = \left(A + B\varepsilon^{p^n}\right)\left(1 + C\ln\dot{\varepsilon}^*\right) \tag{2.26}$$

Another material model suitable for modeling metallic materials is the LS-DYNA implemented material *MAT_018_POWER_LAW_PLASTICITY. This is an elasto-plastic material assuming a power law hardening rule, including strain rate effects using the Cowper and Symonds model [40]. The constitutive relation of the material is given in Equation (2.27), where k and n are material parameters describing the plastic hardening, ε_{yp} is the elastic strain until first yield and C and p are parameters related to the strain rate effects. $\bar{\varepsilon}^p$ is the effective plastic strain and $\dot{\varepsilon}$ is the strain rate.

$$\sigma_y = k(\varepsilon_{yp} + \bar{\varepsilon}^p)^n \left(1 + \left(\frac{\dot{\varepsilon}}{C}\right)^{1/p}\right) \tag{2.27}$$

For modeling fluids, the LS-DYNA material *MAT_009_NULL is common. The material definition requires an equation of state to be defined, but does not calculate deviatoric stresses. Any deviatoric stresses must arise from the viscosity, which is not necessary to define. The material model has no shear stiffness [40].

Equation of State

In liquids and gasses, the pressure is typically highly dependent on the compression. The material description is therefore dependent on an equation of state, hereafter EOS, which describes the pressure as a function of the volumetric compression. The internal energy per volume is also an important factor for the pressure.

During slamming, the water is compressed by the impact. The pressure due to compression is well described by the Gruneisen EOS as defined in Equation (2.28) [2]. Parameters c, S_1, S_2, S_3 and γ_0 as well as initial internal energy E_0 are material specific. The non-dimensional parameter μ is defined in Equation (2.29) as the ratio of the current and initial density ρ and ρ_0, respectively.

$$p = \frac{\rho_0 c^2 \mu \left[1 + (1 - \frac{\gamma_0}{2})\mu - \frac{a}{2}\mu^2\right]}{\left[1 - (S_1 - 1)\mu - S_2 \frac{\mu^2}{\mu+1} - S_3 \frac{\mu^3}{(\mu+1)^2}\right]} + (\gamma_0 + \alpha\mu)E \tag{2.28}$$

$$\mu = \frac{\rho}{\rho_0} - 1 \tag{2.29}$$

Air may be modeled as a perfect gas with no shear strength [2], making the linear polynomial EOS a good fit. This is defined in Equation (2.30), with C_i, i=0,1..,6 as material parameters. The initial internal energy E_0 must be defined for the EOS as well.

$$p = C_0 + C_1\mu + C_2\mu^2 + C_3\mu^3 + (C_4 + C_5\mu + C_6\mu^2)E \tag{2.30}$$

Chapter 3

Drop test of unstiffened plate

Design of offshore structures involve complex interactions of hydrodynamics and structural response, including hydroplasticity. Scaled model tests have been, and are still, a common approach to study these types of effects. The experimental method has been important in the process of understanding hydro-elasticity and -plasticity.

A majority of past experiments have been designed with hydroelasticity in mind. Drop tests conducted for the SINTEF Ocean SLADE KNP project were however designed with hydroplasticity in mind, causing permanent deformations of the impacting structure. While giving experimental insights to the process, these experiments are also valuable as verification of analytical and numerical methods. In this chapter, the structural responses of the experimental drop tests will be recreated using numerical simulations as a way of validating the chosen numerical approach.

The SLADE KNP project is a joint research project between SINTEF Ocean and NTNU. The aim of the project is to investigate the structural integrity of offshore structures during extreme wave events. The experimental drop tests of unstiffened plates were performed early in the project to investigate the fluid-structure interaction during elasto-plastic deformations of the plate.

3.1 Experimental test set-up

The drop test was designed to study the deformation of an unstiffened aluminium plate. An aluminium plate was clamped by a steel frame which was bolted to a larger open top box. The box had a rectangular bottom, widening in both directions to the top, and was held in place by a 2.31 m long arm. During the drop, the arm was allowed to rotate about a hinge, causing a rotational motion of the box. Rotation of the box relative to the arm was also possible to allow for impact tests with different deadrise angles. The entire set-up of the drop tests is illustrated in Figure 3.1.

The bottom of the box had a total area of 344 x 500 mm^2. A rectangular aluminum plate with effective width 220 mm was clamped at the center of the box. The plate was 0.6 mm thick and the total mass of the test rig was 139.42 kg. During the tests, the rig was dropped into a basin about 2 m wide, 10 m long and 1.15 m deep [1].

Two 3D-DIC cameras were installed above the box to capture the deformations of the aluminum plate. The plates were spray-pained with a speckle pattern, allowing for DIC tracking of deformations. The cameras were operating at 37 kHz.

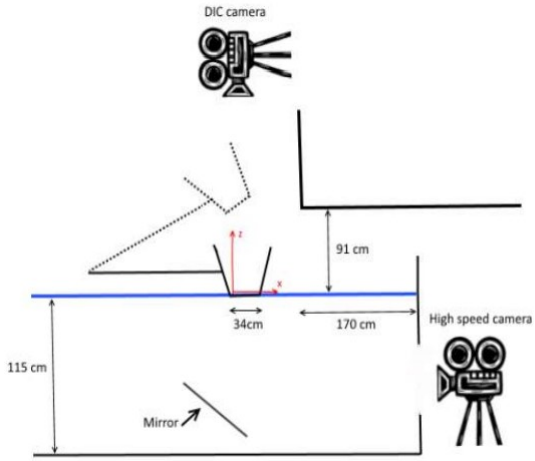

Figure 3.1: Experimental set-up of the drop test, reproduced from Rolland [1].

Twelve drop tests were performed during the experiment, the conditions of which are reported in Table 3.1. The drop rig was rotated upwards about the hinge and

then allowed to fall freely, meaning the different drop heights correspond to different impact velocities. Eight tests were performed with zero deadrise angle between the impacting box and the water surface, and four tests were performed with deadrise angle 4°

Table 3.1: Drop test conditions. Impact velocity calculated by Rolland [1].

Test no.	**Drop height** [mm]	**Angle** [°]	**Impact velocity** [m/s]
1, 2, 3	778	0	3.796
4, 5, 6	443	0	2.873
7	222	0	2.038
8	118	0	1.487
9, 10	444	4	2.699
11, 12	845	4	3.712

3.2 Finite Element Model

A numerical model of the drop tests described in Section 3.1 was created with the aim of recreating the results with highest possible accuracy. However, some simplifications were introduced. Modeling is performed combining a Lagrangian structural model with ALE fluid domains. The modeling procedure is described in this section.

The structural finite element model consists of a steel plate and an aluminum plate. For simplicity, only the bottom of the drop box was modeled. The structural model is illustrated in Figure 3.2. The inner aluminum plate in green has width and length 220 mm, and the outer steel plate in yellow is 340 mm wide and 500 mm long, somewhat modified from reality in order to achieve a regular mesh. Both plates are assumed to be 0.6 mm thick and modeled with Belytschko-Tsay shell elements. The two plates are rigidly connected by merging the contact nodes.

As the steel plate represents the impacting box, deformations of the plate are assumed to be negligible. The steel plate is therefore simplified as rigid, only allowing rigid body motions in the vertical direction. The rigid material description only requires a few material parameters, which are set to the typical values for steel. To account for the weight of the entire drop rig, the density of the steel has been significantly increased. The rigid outer plate also enforces clamped boundary

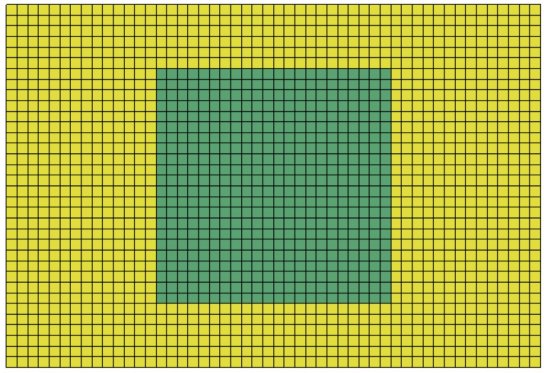

Figure 3.2: Structural model of impacting plates, mesh size 10 mm.

conditions on the aluminum plate.

Material choice for the aluminum plate will be further discussed, with a summary of material parameters for both plates given in Table 3.3.

The fluid domain is modeled three times the length and width of the outer plate, i.e. 1020 x 1500 mm^2. Both the water and air domains are 200 mm high. An illustration is given in Figure 3.3. This was chosen as the optimal domain size after performing a convergence study which will be presented. The air and water are modeled using solid elements with a 1 point ALE multi-material formulation. Both materials are modeled as null-materials with different EOS: air is defined with the linear polynomial EOS while water is defined with the Gruneisen EOS. Material parameters for both materials are defined in Table 3.2, obtained from Truong et. al. [2]. According to recommended practice for modeling fluids in LS-DYNA, hourglass formulation 1 with hourglass coefficient in the range of 10^{-6} to 10^{-4} should be applied. A value of 10^{-6} has been applied here.

The coupling between the structure and the water is defined through the *LAGRANGE_IN_SOLID card. The water domain is defined as the master part while the Lagrangian structures are defined as the slave part set. Penalty coupling is recommended in fluid-structure interaction, and required in coupling with a rigid structure. This is defined with the variable CTYPE, and the default penalty factor PFAC of 0.1 is applied, corresponding to f in Equation (2.20). DIREC set to

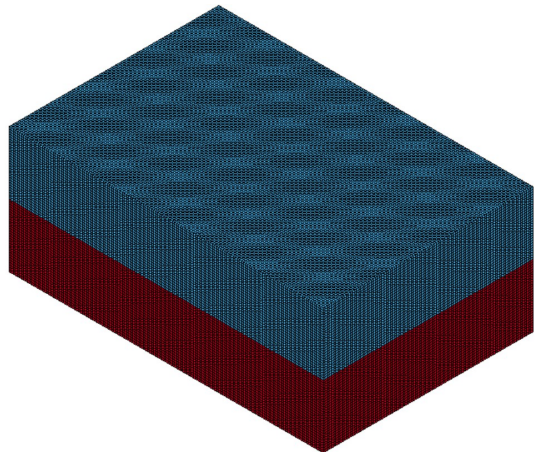

Figure 3.3: Air and water domains.

Table 3.2: EOS coefficients of fluid models, obtained from Truong et. al.[2].

Parameter	**Air**	**Parameter**	**Water**
Density, ρ [kg/m^3]	1.225	Density, ρ [kg/m^3]	1,000
C_0 [MPa]	0.0	Sound speed of fluid, c [m/s]	1,480
C_1 [MPa]	0.0	S_1 [-]	1.921
C_2 [MPa]	0.0	S_2 [-]	-0.096
C_3 [MPa]	0.0	S_3 [-]	0.0
C_4 [MPa]	0.4	γ_0 [-]	0.35
C_5 [MPa]	0.4	First-order volume correction, a [-]	0.0
C_6 [MPa]	0.0	Initial internal energy, E_0 [MPa]	0.2895
Initial internal energy, E_0 [MPa]	0.25	Initial relative volume, V_0 [-]	1.0
Initial relative volume, V_0 [-]	1.0		

2 defines penalty coupling only when the structure compresses water. FRCMIN determines the minimum fraction of ALE material required to enable coupling, which is set to 0.3 as recommended for high velocity impact [40].

Coupling the structure only to the water is defined by setting MCOUP equal to the negative material identity, as is recommended by the LS-DYNA user manual [40]. Three coupling points in both directions for each Lagrangian element is defined by setting NQUAD to 3. Other than what is described here, default values are used as these are considered adequate approaches. The coupling card is illustrated in Figure 3.4.

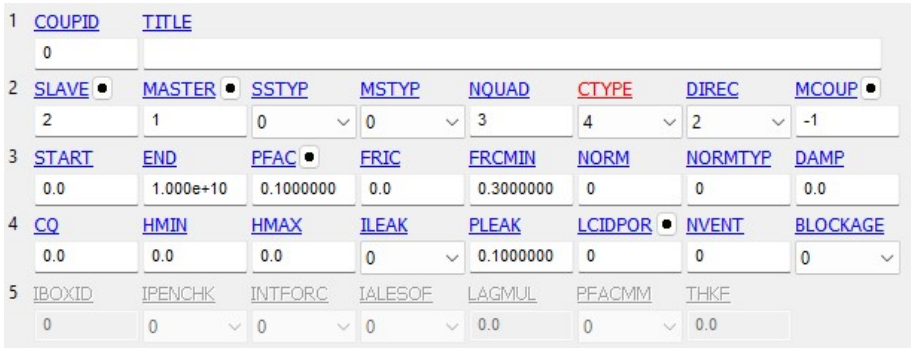

Figure 3.4: *CONSTAINED_LAGRANGE_IN_SOLID coupling card.

In order to simulate the drop tests with a reasonable computational time, the initial position of the plates was set 5 mm above the water surface. This simplification may lead to a reduction in entrapped air which may occur during the initial drop. Instead of simulating the drop, an initial velocity was applied to the structure using the keyword *INITIAL_VELOCITY_GENERATION. This allows the water to decelerate the plate during the impact, an effect which was observed in Abrahamsen et. al. [19]. The impact velocity corresponding to each drop height were calculated by Rolland [1] and are given in Table 3.1. As the plate is only allowed to move vertically, only the vertical velocity component was applied.

Truong et. al. [2] suggests using non-reflective boundary conditions for the outer water domain surfaces, as this will remove the wave impulse reflections caused by the boundaries. In accordance with this, non-reflective boundaries were applied to the outer surfaces of the water part through the *BOUNDARY_NON_REFLECTIVE

keyword, except for the top surface which is connected with the air domain. As this option was explored late in the modeling process, the boundary conditions have only been applied to the angled plate impact.

Modeling and post-processing was performed using LS-PrePost V4.8 x64 2021. Initial simple simulations were ran using LS-DYNA version R10.0. The simulations providing the final results troughtout the thesis were more computationally demanding and were therefore ran on the cluster of NTNU's joint supercomputer *Fram*.

An alternative to LS-DYNA is the numerical solver Abaqus. Although preliminary results from this solver were not satisfactory and the method was abandoned, an explanation of a possible modeling approach of the drop tests in Abaqus is included in Appendix B.

3.2.1 Material model

In addition to the experimental plate drop tests, material testing of the aluminium used for the centre plate in the drop tests was also performed. Tensile tests were performed on specimens produced from the same material as the aluminum plate. The average true stress-true strain curve from the five tests, as given by Rolland [1], is illustrated in Figure 3.5 in blue. A curve fit to the simplified Johnson-Cook material model, given by Equation (2.26), was produced using the MATLAB curve fitting tool. Effects of strain rate hardening were neglected by setting $C = 0$. The fitted material parameters given in Table 3.3 were implemented as the material model for the aluminum plate.

Table 3.3: Material parameters for the aluminium and steel plates, modeled with *MAT_098 _SIMPLIFIED_JOHNSON_COOK and *MAT_020_RIGID.

Parameter	**Aluminium**	**Steel**
Density, ρ [kg/m^3]	2720	1.91E+6
Young's modulus, E [GPa]	72	210
Poisson's ratio, ν [-]	0.32	0.3
A [MPa]	19	-
B [MPa]	127.2	-
C [-]	0	-
n [-]	0.4051	-

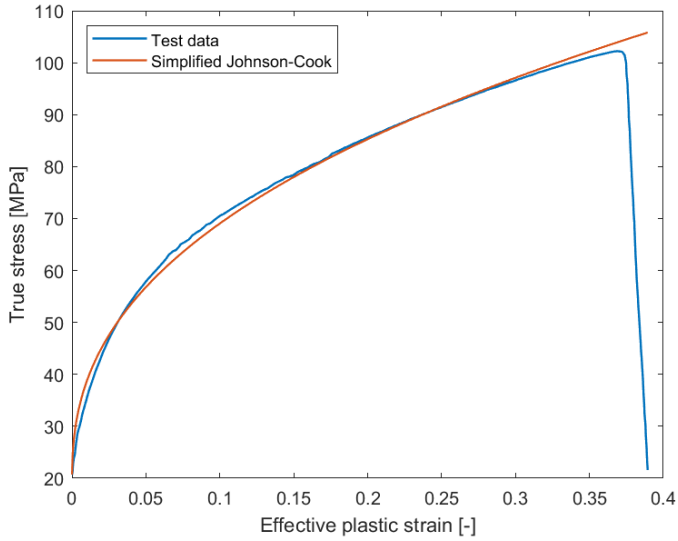

Figure 3.5: Stress strain relationship from material testing and fitted Johnson-Cook model.

3.2.2 Convergence study

The mesh size used for modeling and the size of the fluid domains are two factors that greatly affect both the accuracy of the results of the numerical simulation as well as the computational effort. Convergence studies have therefore been performed, finding the minimum requirements for both cases.

Cheon et. al. [24] gave an extensive study of different factors affecting numerical fluid-structure interaction simulations. It was found that the ideal discretization of the problem used the same mesh size for the structural and fluid meshes. Therefore, convergence has only been studied using the same mesh size for all meshes.

Mesh sizes of 5, 5.5, 7.3, 10, 20 and 50 mm have been used in simulations with impact velocity 2.038 m/s. The results of the convergence study are illustrated in Figure 3.6(a). The results are found to be sufficiently converged for a mesh size of 5 mm, with coarser meshes overestimating the response.

The extent of the fluid domain has also been considered in a convergence study, given in Figure 3.6(b). An impact velocity of 3.796 m/s and mesh size 10 mm for both structural and fluid meshes were used in the study. The size of the fluid

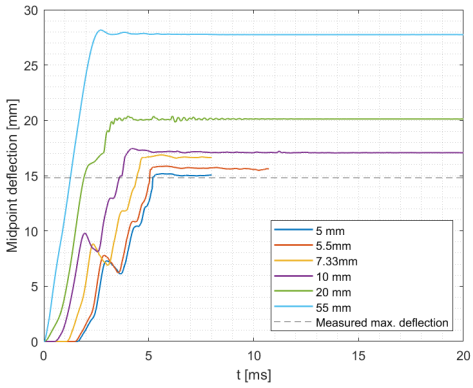

(a) Mesh size

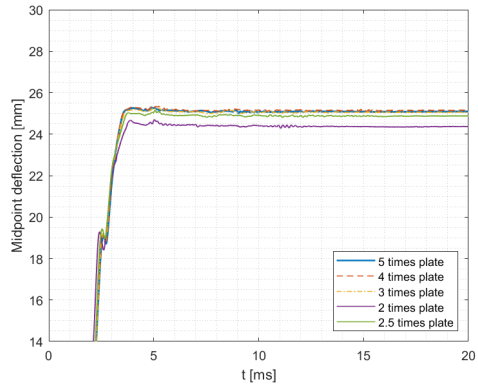

(b) Spacial extent of fluid domains

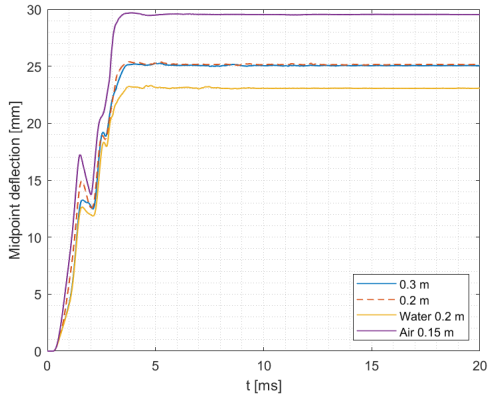

(c) Fluid domains depth

Figure 3.6: Convergence studies for plate drop test.

domains have been defined with regards to the outer measurements of the steel plate, with the plate being located at the centre of the domains. It is apparent that the solution is fully converged when the fluid domains extend more than three times the length and width of the outer plate. This has therefore been chosen as the domain size in further analysis.

For the previous studies, the depth of both the air and water was kept constant at 0.3 m. Figure 3.6(c) illustrates the effect of a reduction in depth to 0.2 m. Keeping the same depth for both domains, the results are sufficiently converged with depth 0.2 m. The effect of keeping one of the domain heights at 0.3 m and changing the

height of the other domain is also illustrated in the figure. Based on the results illustrated, the ideal fluid domain size was taken as 1020 x 1500 x 200 mm^3 for both the air and water domains.

3.3 Results

The midpoint deflections of the plate with zero deadrise angle from experiments and simulations are illustrated in Figure 3.7. For the drop heights with repeated tests, the impact with maximum deflection is illustrated. The maximum deflections from simulations and the experimental drop tests are also reported in Table 3.4. For the two middle heights, the numerical simulation gives a good estimation of the experimental results, while for the highest and lowest drop heights, there is a larger discrepancy between the results. It is observed that the simulations do not yield an elastic recovery after the occurrence of maximum deflection as the experimental results do.

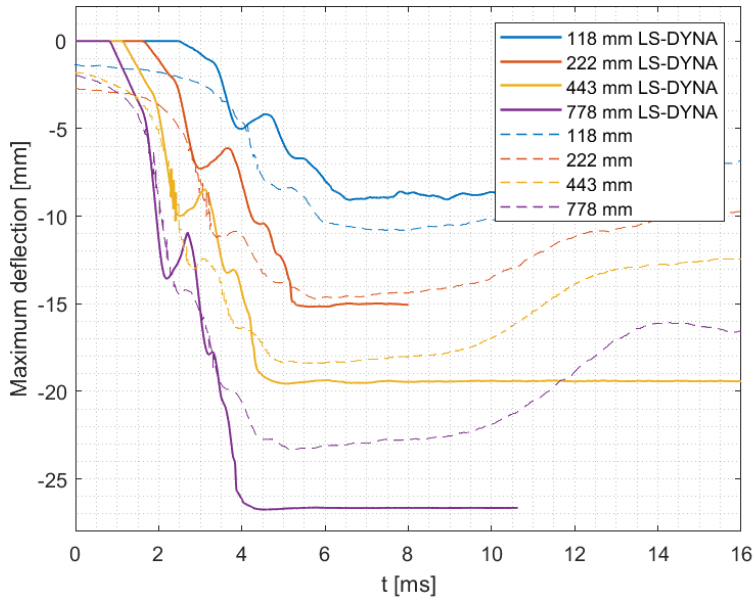

Figure 3.7: Maximum plate deflection from numerical simulations and experimental drop tests for flat plate. Experimental results reproduced from Rolland [1].

Deflection curves, illustrating the deformation pattern of the aluminium plate due

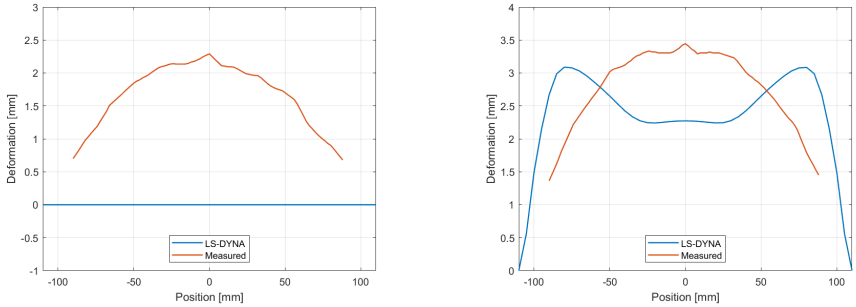

(a) t = 0.60 ms

(b) t = 1.67 ms

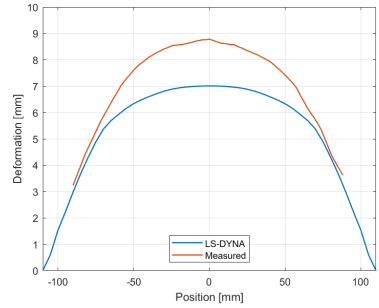

(c) t = 2.12 ms

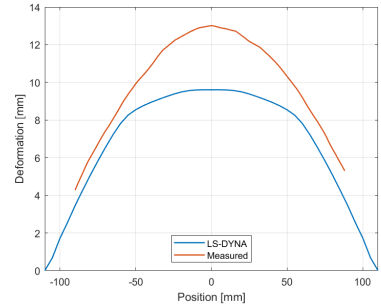

(d) t = 2.75 ms

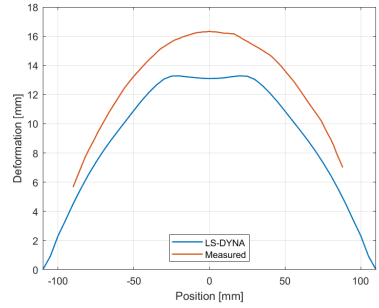

(e) t = 3.83 ms

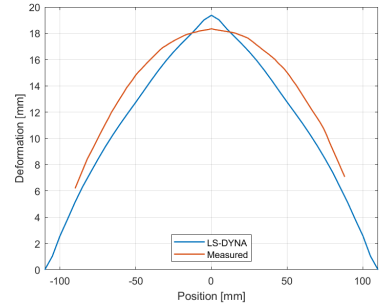

(f) t = 6.00 ms

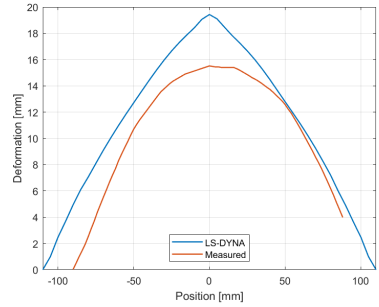

(g) t = 10.86 ms

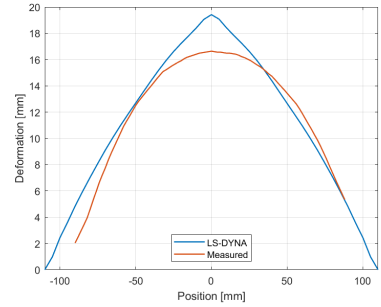

(h) Permanent deformation

Figure 3.8: Deflection profiles of the middle of the flat plate from experimental drop tests and numerical simulations. Experimental plots reproduced from Rolland [1].

Table 3.4: Maximum deflections from experimental and numerical drop tests of the plate.

Drop height [mm]	**Imp. angle** [°]	**Exp.** [mm]	**Numerical** [mm]	**Error** [%]
118	0	10.82	9.07	-16.2
222	0	14.77	15.17	2.7
443	0	18.41	19.56	6.2
778	0	23.41	26.75	14.3
444	4	18.12	16.96	-6.4
845	4	25.00	24.25	-3

to a 443 mm drop height, are reported in Figure 3.8. Time instances corresponds to the midpoint deformation plot in Figure 3.7. While the experiments measured an initial curvature of the plate at impact, the plate is initially completely flat in the numerical simulation. The numerical simulation underestimates the plate deformation during the initial stages of deformation, while the plate deformations are overestimated at the end. The numerical simulation also finds a sharper deformation mode at the end of the drop.

The maximum deflections of the plate impact with deadrise angle 4° is illustrated in Figure 3.9. The maximum deflections are somewhat underestimated, as given in Table 3.4. However, the simulations give a good estimation of the permanent deformations of the plate. This is confirmed in Figure 3.10(h).

The deformations of the centerline of the plate during the angled impact is illustrated in Figure 3.10. As was observed for the flat plate impact, the plate has an initial curvature before impact in the experiments which is not reproduced in the numerical simulations. There is some discrepancy in the deformation modes during the initial stages of impact, with a better fit during the later stages and for permanent deformation.

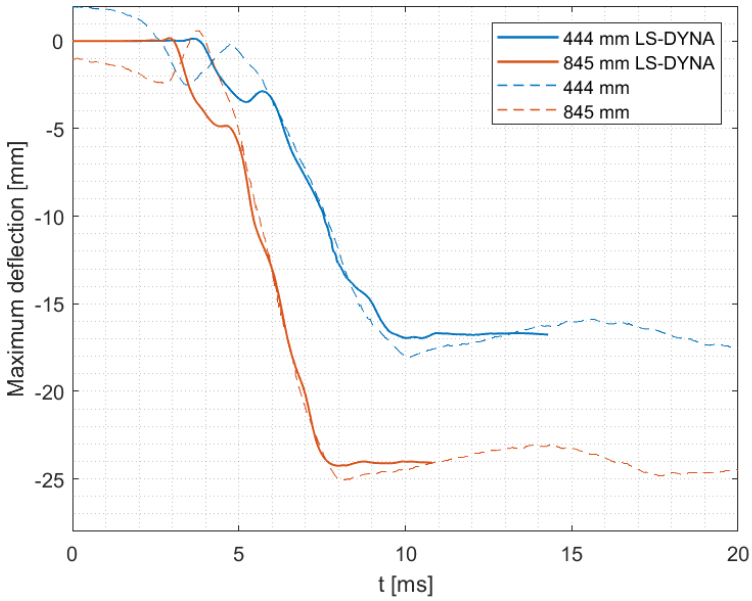

Figure 3.9: Maximum plate deflection from numerical simulations and experimental drop tests with deadtise angle 4°. Experimental results reproduced from Rolland [1].

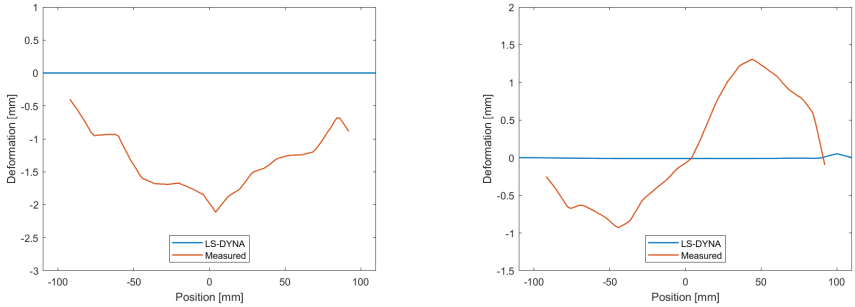

(a) Initial t = 0.0 ms

(b) t = 2.38 ms

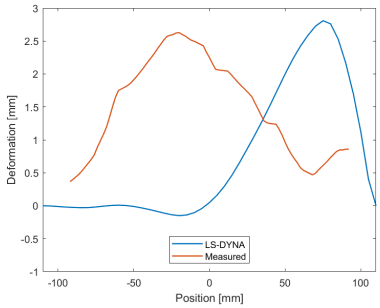

(c) t = 3.48 ms

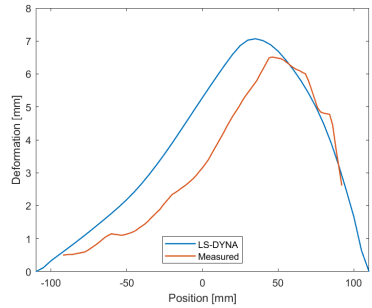

(d) t = 5.58 ms

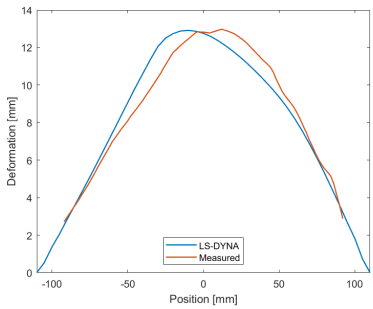

(e) t = 7.78 ms

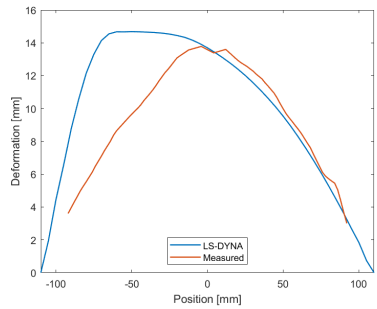

(f) t = 8.88 ms

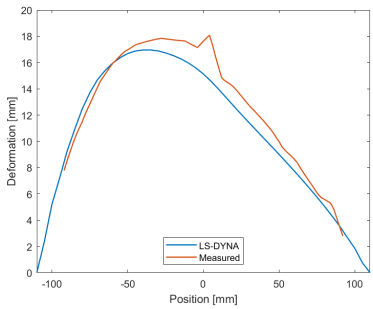

(g) t = 10.48 ms

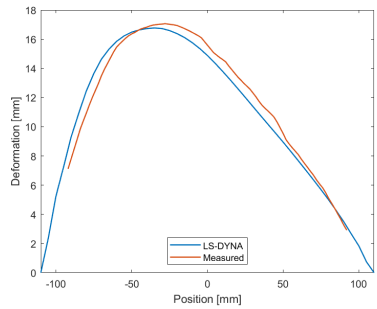

(h) Permanent deformation

Figure 3.10: Deflection profiles of the middle of the plate with dead angle 4°, from experimental drop tests and numerical simulations. Experimental plots reproduced from Rolland [1].

3.4 Discussion

The numerical simulations of flat impact were in good agreement with the results of the experimental drop tests for heights 221 mm and 443 mm, giving good estimations of the maximum deflections of the plate. For the highest drop height, there was however a larger discrepancy between results. For the highest drop height, leakage was observed. This means that the water passed through the plates despite the plates being intact. The recommended remedies for leakage issues in ALE modeling were implemented, but no significant improvement was found. Despite this, the numerical settings were found adequate for use in further modeling, keeping in mind to be aware that leakage issues may arise.

Another reason for the overestimation of deflections for the highest drop height is the deformation mode. Figure 3.8 illustrated the centerline deformation of the plate. While the numerical simulation accurately described the deformation of most of the plate, the deformation of the midpoint and the closest surrounding area was overestimated. The numerical simulation found a quite triangular deformation mode for the plate, while in experiments the plate developed a more sinusoidal deformation mode. This gives reason to the consistent overestimation of deflections reported in Table 3.4. As larger deformations will give a larger curvature of the middle section, this also explains why the effect increases with increasing deformations.

Figure 3.8 illustrated discrepancy between the deformations of the numerical and experimental drop tests. This is however not given too much focus, as the deformation curves illustrate the later stages of impact, while Figure 3.7 illustrated a better fit between the two methods during the initial stages. It should be noted that the lack of initial curvature in the numerical model may affect these results negatively. This is particularly visible for the deformation mode illustrated in Figure 3.8(b) which is not similar to any deformation mode observed in the experimental results.

It should be noted that for the lowest drop height, the numerical simulation underestimates the maximum deflection. When studying the simulations of this drop test, it was found that the impact lead to localised deformations elsewhere than the centre of the plate due to numerical instabilities. The instabilities become apparent

after about 6 ms, as before this the drop corresponds well with the other simulations. This explains why the midpoint deformations of the plate with lowest drop height is underestimated and why a less stable deformation of the midpoint may be observed during the late stages of the impact.

Figures 3.9 and 3.10 confirm good agreement between numerical and experimental results also for the angled plate impact. While the flat impact mostly overestimated the deflections of the plate, the numerical simulations of the rotated plate slightly underestimated the maximum deflections. There was however very good agreement between the numerical simulations and permanent deflections of the plate, clearly illustrated in Figure 3.10(h).

There was one significant difference between the flat plate model and the rotated plate model: for the impact with deadrise angle 4°, non-reflective boundary conditions were applied to the outer surfaces of the water domain. While the simulation of flat plate impact gave acceptable results without these boundary conditions, the rotated plate model found this necessary for good agreement. A reason for this may be that the domain convergence study was performed for the flat plate model. In addition, an angled plate causes a less symmetric fluid flow and more horizontal motion which may lead to the non-reflective boundary conditions having a more significant role.

Due to the extensive reporting of the experimental drop tests provided in Rolland [1], the numerical model was created based on data provided there. Part of the work included calculations of initial impact velocity for the different drop heights. The experiments have also later been reported by the scientists responsible in Abrahamsen et. al. [19]. This publication included an explanation of their numerical model, including calculated impact velocities used in the simulations. The impact velocities calculated in Abrahamsen et. al. are on average 0.2 m/s higher than those calculated by Rolland, giving an increase of 8% in each case. The discrepancy seems to stem from different calculations of rotational moment of inertia of the drop rig. There was also some discrepancy in the reported mass of the drop rig, which was somewhat overestimated in Rolland. Although values given in Abrahamsen et. al. are considered more trustworthy, the discrepancies were discovered to late to study further. It would however be interesting to study if the data reported in Abrahamsen et. al. would yield more accurate results.

Only vertical motions of the plate were allowed. In reality, due to the drop rig being held by the arm, the motion of the plate at water entry is somewhat rotational. This means that in addition to the vertical velocity which was reported in Table 3.1, the plate also has an initial horizontal velocity. This could be modeled in LS-DYNA by introducing a revolute joint constraint with the keyword *CONSTRAINT_JOINT_REVOLUTE. The simplification of only introducing verical motion is however found to be reasonable as the results nevertheless correspond well with experimentally measured results.

The material model of the aluminum plate may be considered somewhat of an uncertainty in the numerical model. While the experimental results illustrate a significant elastic recovery after maximum deflection, this is not observed in the numerical results. This may be caused by an underestimation of the elastic properties of the material. This is supported by the material model calibrated in Abrahamsen et. al. [19] having a yield stress of 27 MPa. Furthermore, modeling in later chapter utilises a more reliable material model, causing elastic recovery in the structural response.

According to Greenhow and Yanbao [3], interaction effects with air may be of significance for plate impacts with deadrise angle less than 3°, as is the case here. In these simulations, air is included but not coupled to the structure, meaning that it is present but allowed to flow freely trough the plate. This gives a more realistic modeling of the free surface of water, but is clearly not realistic with regards to the structure. In order to study the effect of air in these drop tests, it would be interesting to run simulations where the structure is also coupled with the air, as well as simulations using void instead of air. These studies have however been left for further work due to time restrictions.

Chapter 4

Drop of rigid cylinder

The Odfjell Oceanwind floating wind foundation concept Deepsea Semi received Approval in Principle in February 2022 [41], confirming the feasibility of the concept. The Deepsea Semi foundations are designed for water depths between 60 and 1300 meters and wind turbines up to 15 MW and will be mobile. The concept consists of three cylindrical columns connected by a truss.

Figure 4.1: Oddfjell Offshore floating wind turbine concept, reproduced from [6].

One of the columns will be studied with regards to slamming impact. The columns have previously been analysed by the in-house engineering team at Odfjell Oceanwind according to DNV OTG-14, which found unacceptable damage to the structure. The aim of this study is therefore to assess the validity of the DNV guidance by numerical simulations of the slamming impact.

A 8 m high section of one of the three columns shall be analysed. The diameter of the column is 12 m, with a constant thickness of 25 mm. The column is stiffened by flat bar ring stiffeners with 1 m spacing, web height 500 mm and thickness 25 mm. The geometry is illustrated by the finite element model in Figure 4.2.

DNV OTG-14 [7] gives design pressures to be applied to a 3 x 3 m^2 panel of the structure. The maximal peak pressure given in the OTG is 1.3 MPa. DNV RP-C205 [35] gives the relation in Equation (4.1) between the space averaged pressure p and impact velocity V. ρ_w is the density of water and C_p is a pressure coefficient. For smooth cylinders, C_p should not be less than 5.15 and for flat plates, it should not be less than 2π. Using the flat plate approach, a peak pressure of 1.3 MPa corresponds to an impact velocity of 20.1 m/s. The wave impact velocity used in this study is therefore chosen as 20 m/s.

$$p = 0.5\rho_w C_p V^2 \tag{4.1}$$

The wave impact will be simplified to a drop of the cylindrical column into initially still water. Analytical slamming models are commonly based on a flat plate or beam impact, which is not a reasonable assumption for a cylinder. However, there exists some analytical models for estimating the pressures on a rigid cylinder during slamming impact such as the Greenhow and Yanbao extension of Wagner theory. An initial rigid model of the cylindrical column has therefore been studied to validate the numerical modeling. The deformable model will be studied further in Chapters 5 and 6 with regards to a coupled drop test and stationary pressure loading, respectively.

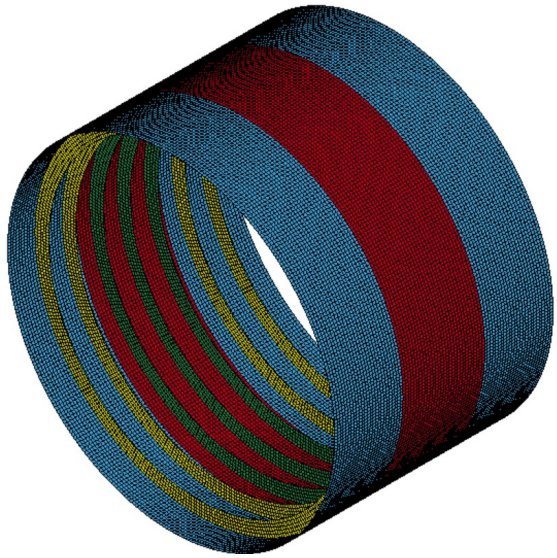

Figure 4.2: Structural model of the cylindrical column, mesh size 100 mm.

4.1 Finite Element Model

The geometry of the structural model is illustrated in Figure 4.2, with dimensions as given in the chapter introduction. The middle and outer sections of the cylinder are modeled separately, as are the stiffeners, as only the middle section will be coupled to the water. The cylinder is modeled with Belytschko-Tsay shell elements and is made rigid by use of material model *MAT_020_RIGID. The same steel model used in the deformable case is implemented, with density 7850 kg/m^3, Young's modulus 204 GPa and Poisson's ratio 0.3. All the rigid parts are connected by merging the intersecting nodes and applying the keyword *CONSTRAINED_RIGID_BODIES. The other parts are then defined as slaves of the middle section of the cylinder.

The velocity is assumed to be constant throughout the drop. The keyword *BOUNDARY_PRESCRIBED_MOTION_RIGID is used to ensure this. A drop velocity of 20 m/s is applied.

The fluid domain is defined with the same length as the cylinder, i.e. 4 m. The width of the domain is two times the diameter and the depth of both the water

and air domains are equal to the radius. The influence of domain size is further investigated for the deformable cylinder. Both the air and water are defined in the same manner as in Section 3.2, with the exception of the water density. Sea water is modeled instead of fresh water, increasing the density to 1025 kg/m^3.

The same coupling between structure and water as applied in Section 3.2 is also applied here. As previously mentioned, only the middle section of the structure is coupled to the water. The non-reflective boundary conditions applied in the angled plate impact are also applied for the cylinder model. Boundary conditions are defined for the five of the water surfaces, excluding the free surface connected to the air domain.

Wagner's slamming model presented in Section 2.1 gives the slamming pressures on rigid structures, so it is desirable to measure the pressures on the cylinder. This is defined through *DATABASE keywords. Two options are available: *DATABASE_FSI and *DATABASE_FSI_SENSOR. Through *DATABASE_FSI, history values such as pressure and force are averaged over a set of elements. *DATABASE_FSI_SENSOR gives history variables such as displacement and pressure at the center of a single element. Both types of databases are requested for comparison with analytically calculated values, with results presented in files *dbfsi* and *dbsensor* respectively.

4.2 Estimated pressure curves based on Wagner's analytical model

Wagner's analytical model for calculating slamming pressures on a rigid body was presented in Section 2.1. Greenhow and Yanbao's [3] solution for the wetted surface length of a cylinder was also presented, giving the ratio between water entry velocity and wetted surface change rate μ and the non-dimensional time Vt/R as functions of the non-dimensional wetted surface length c/R.

The infinite series presented by Greenhow and Yanbao have been calculated numerically using MATLAB. The terms have then been scaled according to the cylindrical column model and used in Equation (2.3) for pressure calculations. Further explanation and the MATLAB code is included in Appendix A.

The pressure distribution on the cylinder is illustrated in Figure 4.3, with the x-

coordinate measured from the centerline. The pressures increase towards the intersection between the wetted surface and the free surface of the water, with an infinite pressure at the intersection. The magnitude of the pressure decreases with time, being the largest at the initial impact.

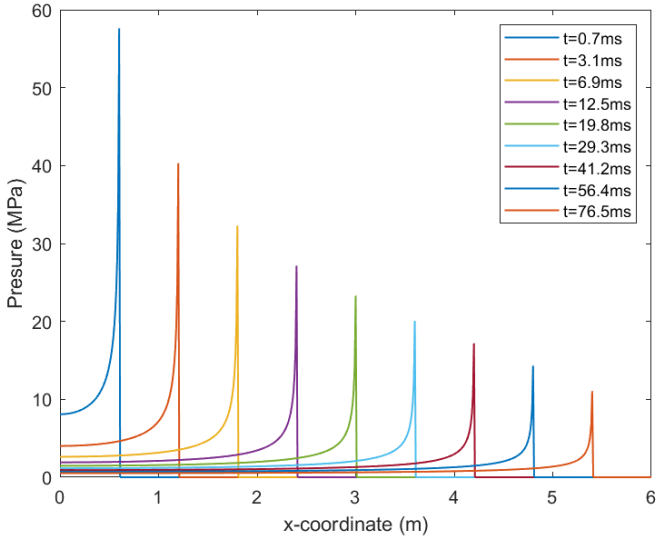

Figure 4.3: Analytical pressure distribution on rigid cylinder at different stages of the impact.

The time history of the pressure at the center of the cylinder and 1 m away from the center is plotted in Figure 4.4. As it takes some time for the second location to enter the water, there is about 2 ms delay before the peak for location 1 m.

Equation (2.3) gives infinite pressure at the intersection between the wetted structure and the free surface. The peak pressures depend highly on how close to the instantaneous wetted length $c(t)$ the discrete location x_i is. The peak values observed in Figure 4.4 should therefore not be given too much consideration. It is however more interesting to study the pressure impulse, i.e. time integral of the pressure or the area under the graph, and the pressure development after the peak.

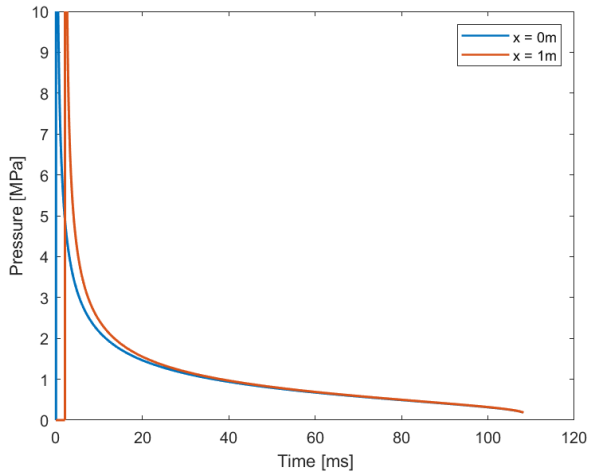

Figure 4.4: Pressure time history at different locations on the cylinder.

4.3 Results from drop simulation

Pressure history outputs from the *dbfsi* file are defined in Figure 4.5. Two sets of elements are defined: the strip along the bottom centerline of the middle section and the four central elements at the center stiffener. The strip pressure resembles a smoothing of the strip pressures, illustrating the same trend but with smoothed oscillations. The peak of the strip pressure is about 1 MPa lower than the local element pressure.

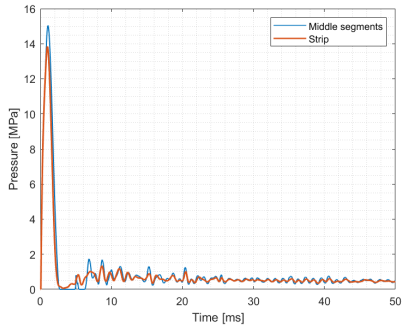

Figure 4.5: Pressure time histories from *dbfsi*.

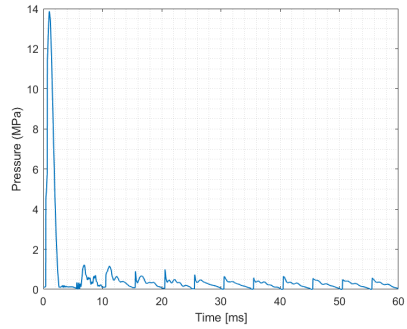

Figure 4.6: Pressure time history from *dbsensor*.

The pressure time history output from the *dbsensor* file is illustrated in Figure 4.6, for a sensor located at the bottom middle element. The initial peak corresponds to the length averaged pressure peak observed from the *dbfsi* file. Instead of having an ocsillatory pressure at later stages of the impact, *dbsensor* reports several peaks in pressure with a much lower magnitude, all tending to zero before the onset of the next peak.

The pressure time histories presented in Figure 4.4 are more similar to the pressures in Figure 4.5 than Figure 4.6. The pressure impulse from the *dbsensor* time history is also much smaller than the impulse calculated from the analytical solution. According to Cheon et. al. [24], the spacially averaged pressures are considered much more representative for the structure as this smooths the spacial fluctuation. Only the *dbfsi* pressures are therefore presented in the further findings. The middle elements pressures pressures are plotted with the analytical results in Figure 4.7. Pressures are evaluated at the centerline and 1 m from the centerline. The LS-DYNA results have been shifted so that $t = 0$ represents the cylinder entering the water in all pressure curves.

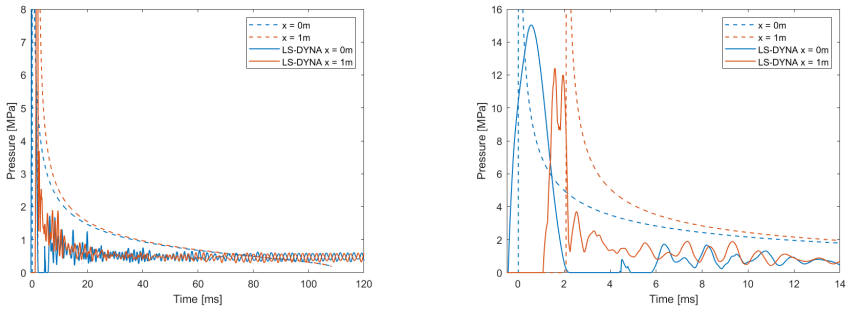

(a) Time history overview **(b)** Initial peak details

Figure 4.7: Pressure history from numerical and analytical solution.

The initial impact pressures at x=0 are illustrated in Figure 4.7(b). It is apparent that the rise time until maximum pressure is longer in the numerical simulation than in the idealized model. The duration of the pressure peak is also longer, and the maximum pressure occurs half a millisecond later. Calculated impulses are given in Table 4.1, with a discrepancy of only 0.3 kPa·s between the numerical and analytical impulse. This is an error of 0.2%.

Figure 4.7(b) also gives the peak pressure at a distance of 1 m from the center of the cylinder. While the duration of the pressure peak are in the same range for both pressure histories, the peak in the numerical simulations is lower. The high pressures are sustained for a much shorter period, as is also true for pressures at x=0 m. This leads to a lower pressure impulse in the numerical simulation than from the theoretical model, a total discrepancy of 5.4% relative to the analytical impulse. The first peak occurs about half a millisecond earlier in the numerical simulation than in the analytical results.

Table 4.1: Comparison of pressure impulses from analytical and numerical solutions. Location defined relative to centerline.

Location [m]	**Analytical** [kPa·s]	**Numerical** [kPa·s]	**Error [%]**
0	122.8	123.1	0.2
1	121.0	114.5	-5.4

The pressures acting on a 3 x 3 m^2 panel at the bottom of the middle cylinder section is reported in Figure 4.8. The peak pressure is 5.75 MPa, with a pressure impulse of 110.8 kPa·s acting on the panel.

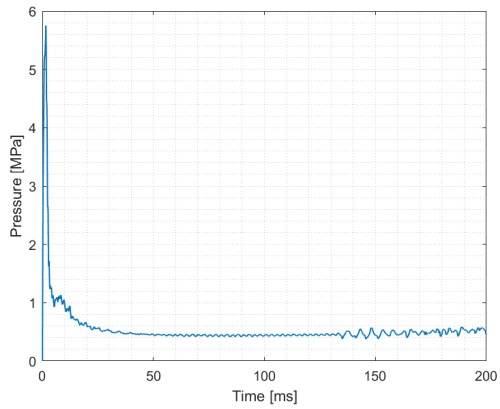

Figure 4.8: Pressure time history acting on 3 x 3 m^2 panel of rigid cylinder.

The flow of water as a result of the rigid cylinder drop is illustrated in Figure 4.9, where the water is illustrated in blue and the air in red. The figure illustrates the formation of water jets at the intersection between the structure and the free surface.

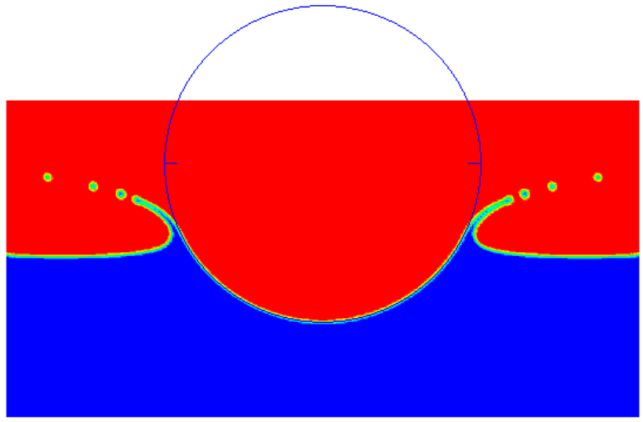

Figure 4.9: Water flow as a result of rigid cylinder drop.

4.4 Discussion

The extension of Wagner's theory presented in Greenhow and Yanbao is found to overestimate the pressures on the cylinder but give a quite good representation of the spacial distribution. It was therefore expected that the analytical model would somewhat overestimate the pressure impulse calculated from the numerical simulation. This is observed for the pressure measurements 1 m from the centerline, where the analytically calculated impulse is 6.5 kPa·s higher than the numerical impulse. At the centerline, there is however only 0.3 kPa·s separating them, with the numerical impulse being slightly larger. While this slight underestimation is negligible, a reason may be the validity of the analytical model at the initial impact, when $c(t) = 0$ and $\frac{dc}{dt}$ approaches infinity. Nevertheless, the results are found to be satisfactory and the numerical model is considered reasonable for the next stages of analysis.

Another aspect of the theoretical model which is not in accordance with the simulation is the formation of water jets, as illustrated in Figure 4.9. The effect of these water jets are neglected in the analytical method. More advanced approaches using Wagner theory do account for the formation of jets by combining the outer and inner domain equations, for example in Cointe and Armand [12]. While this method yields more accurate results for the hydrodynamic force on the cylinder,

the contribution to the pressure during the initial stages of impact is expected to be low [3].

The impulses from the numerical simulation in Table 4.1 are averaged over the center elements of the cylinder. This is chosen over what is referred to as the strip pressure because the analytical model is based on an assumption of 2D flow. As coupling is only applied to the central section of the cylinder, the flow will have more 3D effects at the edges of the middle section. Due to the symmetry of the problem, the flow at the middle of the cylinder will be the most two dimensional and is therefore expected to be more comparable to the theory than the pressure averaged over the full length. For comparison, the impulses on the strips are 116.4 and 108.3 kPa·s at 0 and 1 m from the centerline, respectively.

As the cylinder is modeled completely rigid in this simulation, no deformations are allowed to form. The oscillations in the measured pressures, as illustrated in Figure 4.7, are more expected for a deformable structure. Even though the motion of the structure is only coupled with the water, this may be the effect of entrapped air. The coupling between the cylinder and the water forces the water to compress. While this coupling is not applied to the air, some air may become trapped between the structure and the water surface, causing time variations in the pressure applied from the water to the structure as the air hinders contact between the coupled surfaces. Despite this, neglecting the coupling to the air is considered reasonable as it was reported in Greenhow and Yanbao [3] that the effect of air pockets during cylinder impact may be considered negligible. To reduce this disturbance in the pressure curves, it would be possible to replace the air with a void.

The *dbsensor* output reports zero pressure on the middle elements of the cylinder for almost 4 ms after the initial peak pressure, as illustrated in Figure 4.7(b). This illustrates a flaw in the modeling technique used: the numerical settings do not seem to be able to model negative pressures, meaning the occurrence of ventilation. In this case, it also gives reason that the pressure measured 1 m from the centerline is not affected, as the deadrise angle is almost 10° and ventilation is less likely to occur. Focus should be given to remedy this issue, but this has been left for further work due to time constraints.

Chapter 3 reported a potential problem with the modeling technique causing leakage of water through the structure. Figure 4.9 illustrates the flow of water as a result of the impact. As no water has penetrated the cylinder, this is not considered an issue in the cylinder drop simulations.

Chapter 5

Drop test of deformable cylinder

The model discussed in Chapter 4 was made rigid in order to compare with results from Wagner's analytical model. In reality, the cylinder will be able to deform during the impact, causing a hydroelasto-plastic coupling between hydrodynamic forces and the structural response. This coupling and the response will be studied further in this chapter.

5.1 Finite Element Model

The model presented in Chapter 4 was somewhat modified in order to make the cylinder deformable. Firstly, a new material model was chosen. Storheim [42] presented a validated material model for offshore steel. The material is defined with a power law plastic hardening as in Equation (2.27), and may be defined using *MAT_018_POWER_LAW_PLASTICITY. Material parameters are presented in Table 5.1.

The cylinder modeled in this study is a section of the full column. Coupling only the middle section of the cylinder to the water is an idealisation of wave impact only in that region. This is expected to cause local damage to the cylinder, leaving the global structure relatively undamaged. Therefore, it is assumed that the surrounding structure, outside the 8 m section modeled, shall remain undeformed also at the end of the drop test. In order to ensure this, the top and bottom edges of the cylinder are made undeformable. The outer sections of the cylinder, in blue in

Table 5.1: Material parameters for steel, used for the column.

Parameter	Steel
Density, ρ [kg/m^3]	7850
Young's modulus, E [GPa]	204
Poisson's ratio, ν [-]	0.3
Initial yield stress, σ_0 [MPa]	338
K [MPa]	758
n [-]	0.19

Figure 5.1, thus provide the central red section with realistic boundary conditions.

In modeling, the top and bottom of the cylinder were made rigid by use of the *CONSTRAINED_NODAL_RIGID_BODY card. This card defines a set of nodes as a rigid body and requires the definition of a node at the center of mass. Rigid body motions may be applied to the entire rigid body by applying a constraint to the center of mass node. Here, a constant drop velocity was defined by applying a vertical velocity of 20 m/s to both the nodal rigid bodies using the SPC, single point constraint, option of the definition card. Only rigid motions in the vertical directions were allowed for the rigid bodies.

As for the rigid cylinder, non-reflective boundary conditions were applied to the outer water surfaces. The full numerical drop test set-up is illustrated in Figure 5.1.

5.1.1 Convergence study

A convergence study was ran in order to determine the ideal mesh size. As previously mentioned, Cheon et. al. [24] found that the ideal solution used the same mesh size for both the structure and the fluid. Mesh sizes of 100, 120, 200 and 500 mm have been applied. Figure 5.2 illustrates the results. All the mesh sizes give reasonably accurate results. Convergence is found for a mesh size of 125 mm or smaller. As some initial tests were ran with a mesh of 100 mm, this mesh size was chosen.

Figure 5.2 also illustrates the effect of fluid domain size. The initial fluid domain was defined based on the dimensions of the cylinder: 8 m long, 24 m wide and 6 m deep for both water and air. It is illustrated in the figure that the width of the

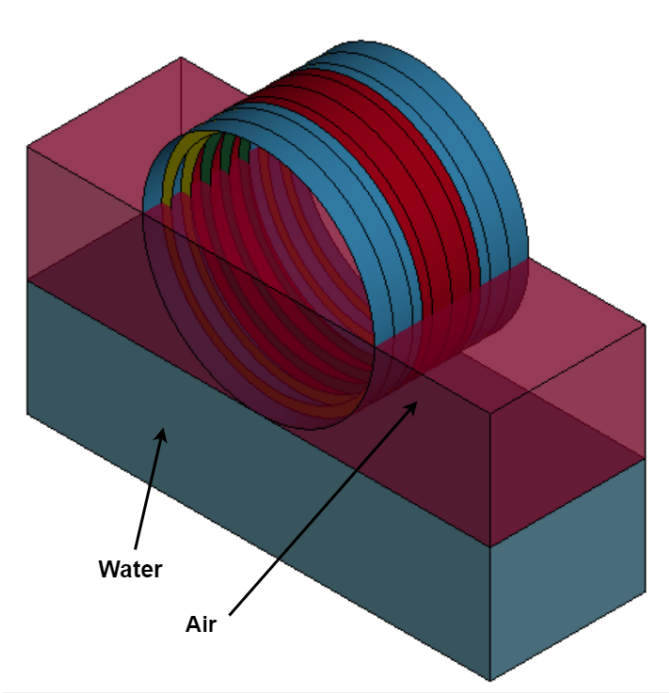

Figure 5.1: Simulation set up for drop test of deformable cylinder.

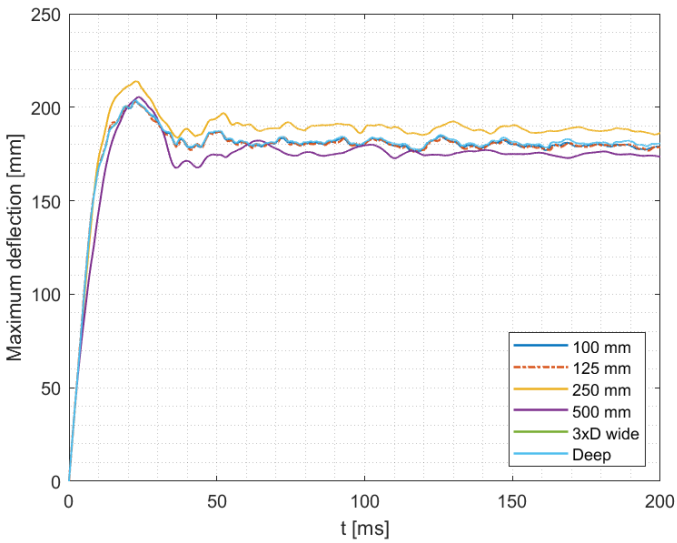

Figure 5.2: Convergence study of the mesh size for the cylinder drop.

domain is sufficient, as increasing the with by 12 m gives no significant difference in response. The figure also illustrates that deeper fluid domains of 8 m depth have little effect on the response of the structure. The chosen fluid domain size of 24 x 4 x 6 m^3 for both air and water are therefore found to be adequately converged.

5.2 Results

The water impact causes significant damage to the cylinder. The vertical deformations of the cylinder are illustrated in Figure 5.3. Most of the cylinder is pushed slightly upwards relative to the rigid edges even though only the central section is coupled to water. The majority of the damage occurs around the centerline. There, the cylinder deforms with six dents in the circumferential direction in the regions between the three central stiffeners. The plate between the next to stiffeners has one dent at the centerline in the circumferential direction. The deformation pattern is symmetric in the length direction.

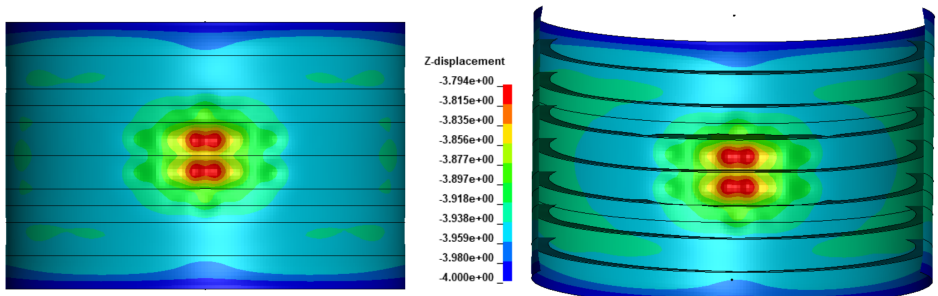

(a) Bottom view

(b) Top view

Figure 5.3: Deformation mode of the deformable cylinder, scaled by 3.

From Figure 5.3, it may be noted that the maximum deformation occurs between the central stiffeners, about 0.3 m from the centerline. In the convergence study in the previous section, the maximum deflection has been measured at the centerline between stiffeners. The absolute maximum deflection of the cylinder is reported in Figure 5.4. The cylinder reaches a maximum deflection of 221.2 mm before settling with a permanent deflection of 205.1 mm.

Pressure histories of the deformable cylinder are presented in Figures 5.5 and 5.6. Figure 5.5 illustrates the *dbfsi* pressures at the central elements located at

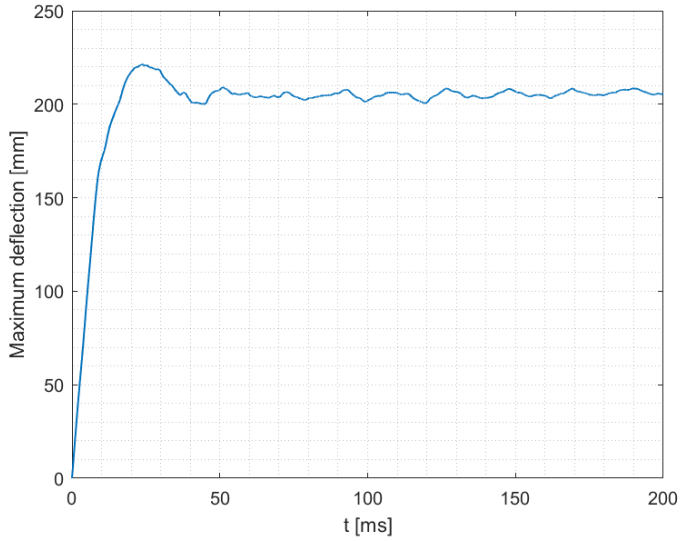

Figure 5.4: Maximum deflection history for the deformable cylinder

the centerline and 1 m away from the centerline. The figure also illustrates the corresponding pressures on the rigid cylinder, showing a significant reduction in pressures on the deformable cylinder. The pressure history on the deformable cylinder is also delayed when compared to the rigid pressure history. However, the deformable cylinder experiences higher pressures for a longer time than the rigid.

Figure 5.6 illustrates the pressure history on a 3 x 3 m^2 panel at the bottom of the cylinder. This panel corresponds to the panel where the design pressure from DNV OTG-14 will be applied. The peak value of the space averaged pressure on the panel is 2.6 MPa, and the impulse from the time history is 110.5 kPa·s.

The von Mises stress distribution is the cylinder is illustrated in Figure 5.7. The maximum stresses occur in the plate at the centerline in the impact region, and are 330.3 MPa. High stresses are also found in other locations of the inital impact zone, as well as along the boundaries. It may be observed that the top and bottom of the cylinder experience higher stresses than the sides.

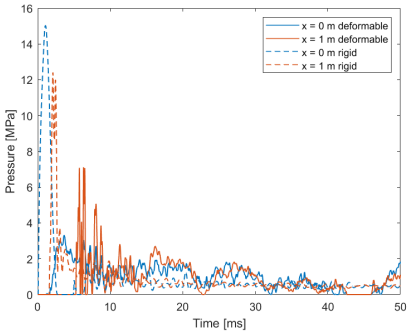

Figure 5.5: Pressure histories of the rigid and deformable cylinder on different locations.

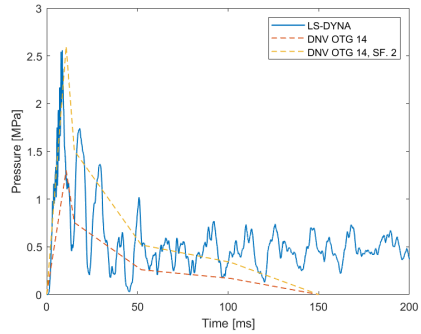

Figure 5.6: Pressure history on a 3 x 3 m^2 panel at the bottom of the middle section of the cylinder. Design pressures discussed in Chapter 6 are also included.

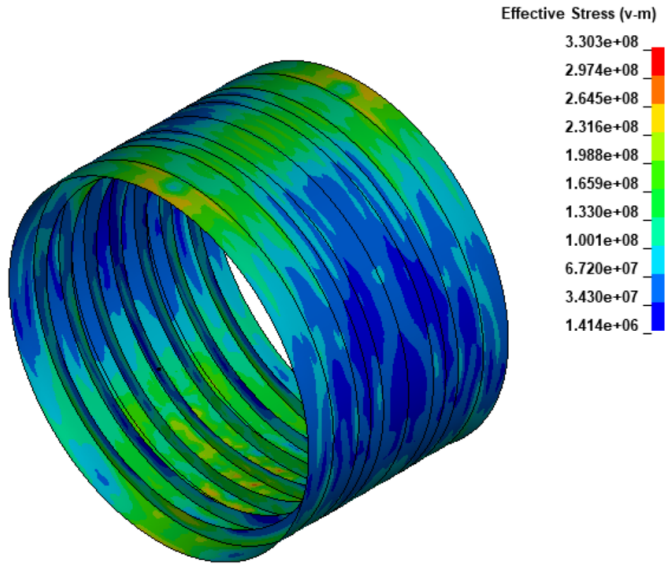

Figure 5.7: Residual von Mises stress distribution at the end of the cylinder drop.

5.3 Alternative models

The impact situation modeled in Section 5.1 shall simulate a wave hitting the column. In the model previously described, the water was only interacting with the middle section of the cylinder. This may be considered an idealization of a jet of water hitting the central section. At the same time, the impacting water must accelerate the surrounding liquid to be allowed to flow in the length direction of the cylinder. While this assumption yields interesting results, it may also be interesting to study the limiting cases as well: a local water jet surrounded by air and infinite water domain.

A local water jet impacting the structure is idealized as a drop test where the water domain only extends over the length of the middle section of the cylinder. The water domain is surrounded by air on both sides, as well as above the water. The set-up is illustrated in Figure 5.8. The water must then only accelerate the surrounding air to be able to move in the length direction of the cylinder, allowing a freer 3D flow than the base case.

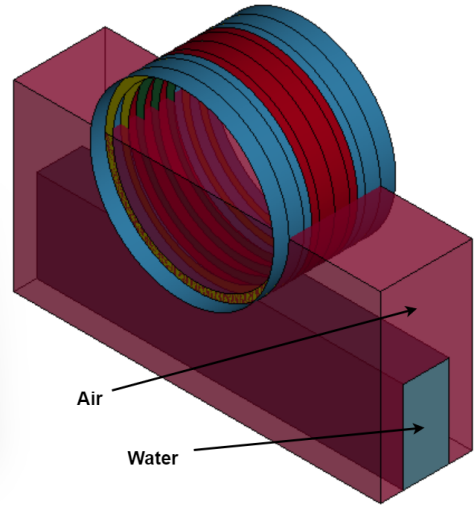

Figure 5.8: Local wave impacting the middle section of the cylinder.

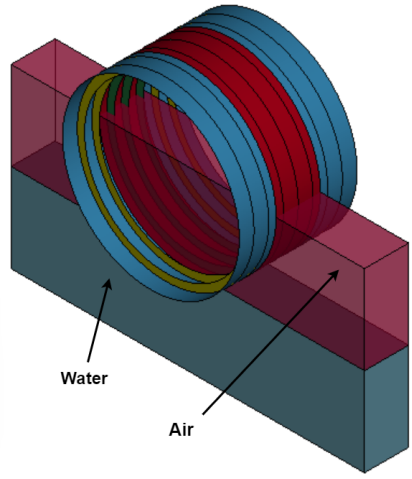

Figure 5.9: Infinite water domain.

An infinite fluid is idealised by ensuring 2D flow. In infinite water, there is an infinite amount of water surrounding the modeled domains which the structure must accelerate, restricting the flow due to impact. This is modeled by defining both the water and air domains the same length as the middle section of the cylinder, as this is where impact is coupled. The x-planes, transverse to the length direction of the cylinder, of the fluid domains are constrained against motion in in x-direction, ensuring no lengthwise flow. The set-up is illustrated in Figure 5.9.

The maximum deflection curves for the two limiting cases are plotted in Figure 5.10. In the local jet case, the permanent deformations are reduced to about 160 mm. It is interesting to note that in this case, a localisation of stresses occur after 70 ms, causing the structure to fail. This is observed by the rapid increase in deflections in the deflection curve.

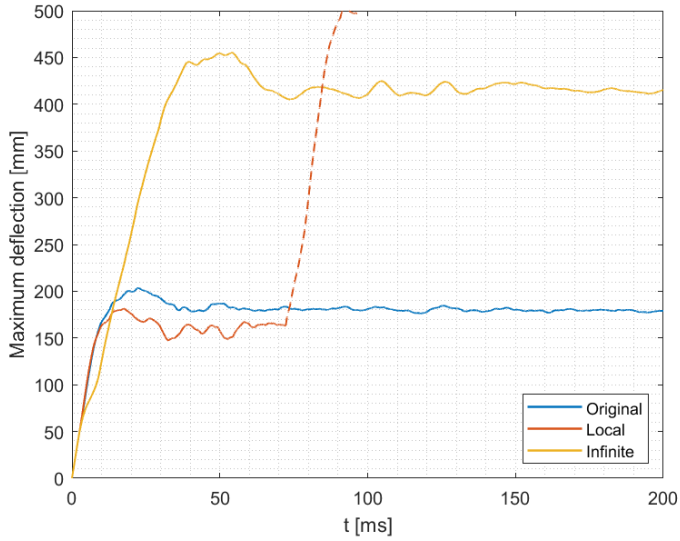

Figure 5.10: Deflection curves for the alternative fluid domains.

The deflection curve for the infinite water domain is also illustrated in Figure 5.10. This limiting case gives a significant increase in permanent deflections from 205 mm to 415 mm. In the infinite fluid domain, the cylinder takes longer to reach maximum deflection, with the peak occuring after approximately 55 ms.

5.4 Discussion

Comparing the pressure history of the rigid and deformable model, there is a significant reduction in pressure on the deformable cylinder. Higher pressures are however sustained for a longer duration. This is particularly visible at the center of the cylinder, where the peak is not significantly higher than the sustained pressure. These findings are in accordance with previous findings by Cheon et. al. [24] and Anglade [28] amongst others.

The cylinder endures a permanent deformation of over 200 mm due to the water impact. This is more than eight times the thickness, and gives visible damage to the structure. There is also damage to the internal stiffeners in the affected region. Several regions of the cylinder have residual stresses in the range of the yield stress. This is expected to reduce the capacity of the structure against further loading, and it would be interesting to perform a residual capacity check in the damaged condition. This has however not been performed due to time restrictions.

Alternative fluid domains are introduced in Section 5.3. The two alternative models presented are considered as limiting cases. The first case corresponds to a jet of water impacting the middle section of the cylinder, while the second case is an idealization of an infinite width of the water domain. An actual wave impact is therefore limited by these two cases, and the actual wave impact response should lay somewhere between the two limiting responses, as illustrated in Figure 5.10.

From Figure 5.10 it is apparent that the largest permanent deformation appears when the cylinder is impacted by an infinite width water domain. When relating this to a wave impact on the column, this would correspond to an infinitely high fluid wall crashing into the structure. This is not a very realistic impact, and as is illustrated by the original model, the structural response would be expected to lay closer to the local water impact response than the infinite width response. The structural response in this simulations is considered very conservative, additionally so due to the constraints introduced to the boundaries.

The most significant damage to the structure occurs for the local water impact case, where the structure fails and deformations increase significantly after 70 ms. This failure is caused by numerical instabilities due to the modeling of the structure, not making them representative of the physical conditions. The deformations be-

fore failure, given by the solid line in Figure 5.10, do however give a reasonable description of the expected deformations in a real world impact.

The impact velocity has been chosen to correspond with the DNV OTG-14 pressure according to Equation (4.1). The DNV OTG-14 is however a ULS design recommendation. In ULS design, safety factors are usually applied both with regards to loading and material uncertainties. If these are applied, the design peak pressure would increase to 1.94 MPa, corresponding to an impact velocity of 24.6 m/s. A higher impact velocity is expected to yield more damage to the structure, causing an even more serious situation than presented in this chapter.

Chapter 6

Pressure impulse on stationary cylinder

DNV OTG-14 [7] specifies design pressures for off shore column stabilised structures like the wind turbine foundation studied in this thesis. Different load levels are given, to be applied to 3 x 3 m^2 and 6 x 6 m^2 panels of the structure. The aim is to ensure safety with regards to ULS design.

The structural response of the cylinder previously discussed from the design pressure will be simulated. The pressure will be applied to a 3 x 3 m^2 panel on the center of the cylinder. DNV OTG-14 gives the highest design peak pressure as 1.3 kPa. The guidelines also specify load levels to be sustained for longer periods. These may be found relative to the peak pressure from a curve. The calculations of the design pressure curve are explained in Appendix C. The resulting design pressure curve is illustrated in Figure 6.1. The pressure impulse of this load is 45.0 kPa·s.

The structural finite element model from Chapter 5 is used, deleting the fluid domains and FSI coupling cards from the model. The constrained nodal rigid body boundary conditions of the top and bottom are kept in place, allowing no rigid body motion of the structure. A 3 x 3 m^2 panel is defined on the middle section of the cylinder and the pressure load is applied using *LOAD_SEGMENT_SET. The

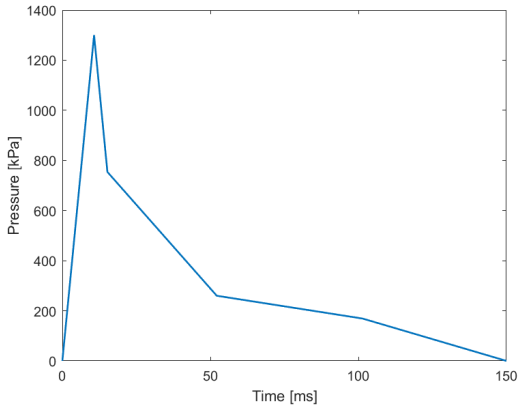

Figure 6.1: Worst case pressure curve, produced based on DNV OTG-14 [7].

pressure history is defined as in Figure 6.1 in linear steps.

6.1 Results of OTG pressure impulse

The deflection history from the OTG-14 pressure load is presented in Figure 6.2. It is apparent that the pressure curve only induces elastic vibrations in the plate, with a maximum value of 24.2 mm. It was however observed that when the pressure load was scaled by two, doubling the pressure at each instance, serious permanent deformations occured. The results of this scaled pressure is also presented in Figure 6.2. The structure then reaches a maximum deflection of 207.6 mm before settling with permanent deformation 177.6 mm.

The permanent deformation pattern for the scaled pressure load is illustrated in Figure 6.3. It can be observed that the plate between stiffeners deforms, causing three dents in the circumferential direction. The maximum deformations occur in the central dent, at the centerline of the cylinder. The response is symmetrical about the central stiffener. From the internal view it may also be observed that the pressure impulse causes damage to the three central stiffeners, bending the two stiffeners on each side of the central stiffener.

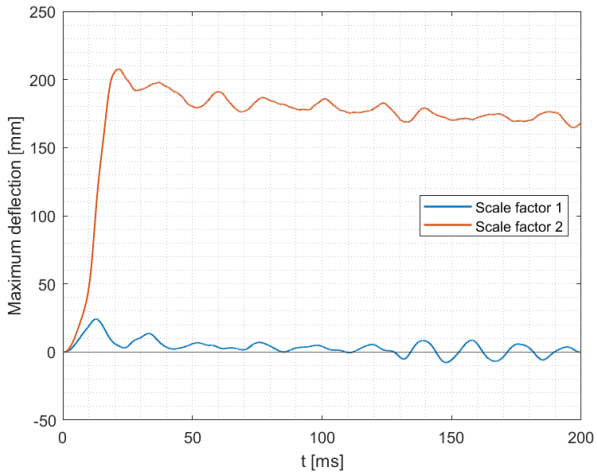

Figure 6.2: Deflections of the cylinder loaded with the DNV OTG-14 pressure.

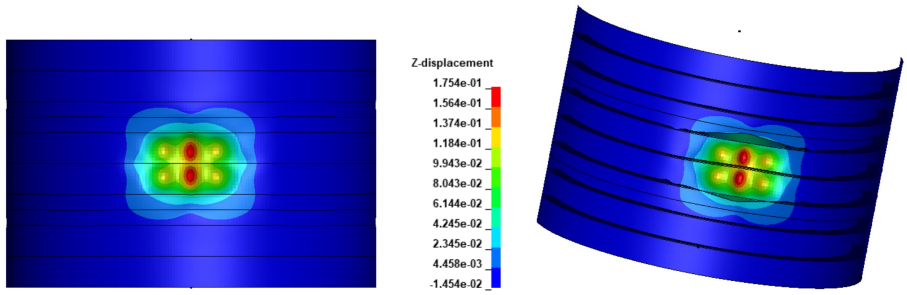

(a) External view **(b)** Internal view

Figure 6.3: Deformation mode when OTG-14 pressures are applied with scale factor 2. Deformations scaled up by multiplicator 4.

6.2 Rigid pressure impulse

A previously common way of studying slamming has been to measure the impact pressure on a rigid structure and later applying the pressure impulse to a deformable structure. This approach removes all effect of hydroelasticity and -plasticity and may be considered an uncoupled approach. In order to illustrate the effect of these phenomena, such a simulation has been performed.

Figure 6.4 illustrates the pressure history on the bottom 3 x 3 m^2 panel of the middle section of the rigid cylinder in blue. The figure also illustrates the fitted

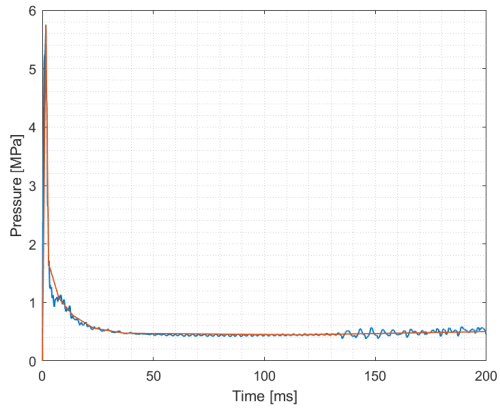

Figure 6.4: Simplification of pressure history on 3 x 3 m^2 panel of rigid cylinder.

simplified curve which was applied to the deformable model. The simplified curve is piecewise linear and was created in a manner so that the total pressure impulse was conserved.

The response of the deformable cylinder is illustrated in Figure 6.5. The maximum deformation is 193.2 mm with a permanent deformation of 154.3 mm.

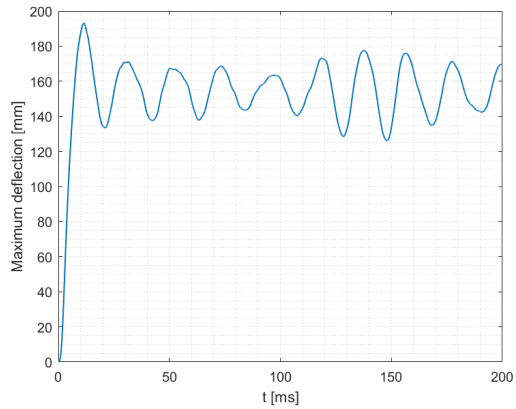

Figure 6.5: Maximum deflection of the cylinder loaded with the rigid cylinder pressure history.

6.3 Deformable pressure impulse

The pressure impulse measured on the bottom 3 x 3 m^2 panel during the impact simulation of the deformable cylinder is illustrated in Figure 6.6 alongside a linearisation. The cylinder, on which this pressure impulse was measured, is identical to the cylinder used in this chapter. A study has therefore been performed as to whether applying the same pressure impulse to the panel would result in the same structural response as found in the coupled drop. As the pressure history has an oscillatory trend, there is some uncertainty tied to the linearisation, but this has been performed so that the total impulse is conserved. The linearised pressure has been applied to the cylinder in the same manner as the previous two cases.

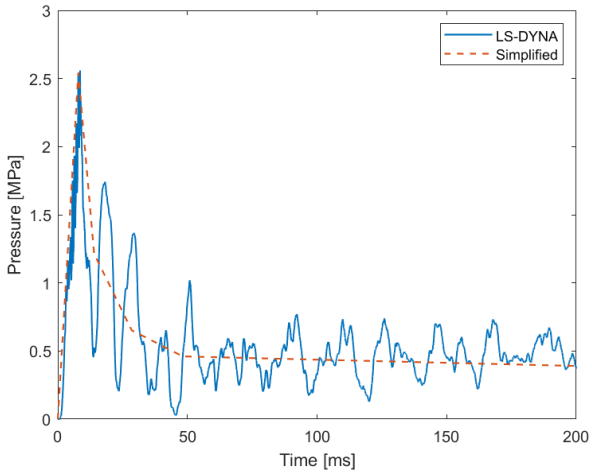

Figure 6.6: Simplification of pressure history on 3 x 3 m^2 panel of deformable cylinder.

The response of the stationary deformable cylinder due to the measured dreformable pressure impulse is illustrated in Figure 6.7. The maximum deformtaion of the cylinder is found to be 132.4 mm. The perament deformations of the structure are 102 mm, with elastic vibrations with amplitude 15 mm.

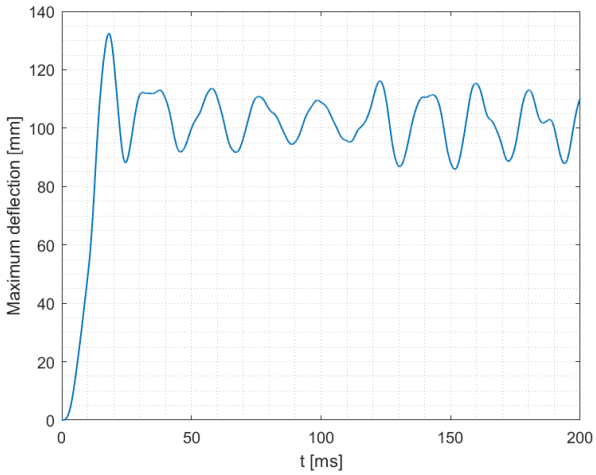

Figure 6.7: Maximum deflection of the cylinder loaded with the deformable cylinder pressure history.

6.4 Discussion

Figure 6.2 illustrates that the OTG design pressure only causes elastic vibrations of the cylinder and no permanent deformations. Although the pressure curve excludes hydroelastic and -plastic effects, it is meant to give a good introductory pressure history for design applications. The drop simulation, with impact velocity calculated based on DNV recommendations, gives significant damage to the structure, as illustrated in Chapter 5. The calculations of drop velocity also neglects the usual ULS load and material safety factors. Inclusions of the safety factors gives an impact velocity of 24.6 m/s which is expected to cause even more severe damage to the structure. Therefore, the design pressure curve is found to significantly underestimate the structural response.

An interesting finding is however the structural response of the scaled design pressure. Doubling the pressure curve, the peak pressure becomes 2.6 MPa and the pressure impulse becomes 90 kPa·s. The impulse is much closer than the measured impulse on the 3 x 3 m^2 of the drop test, as is the structural response. Although also the scaled pressure somewhat underestimates both maximum and permanent deformation from the drop test, it is a much better approximation than the unscaled

design pressure. The scaled pressure impulse also gives a deformation history similar to that found in the drop test. During repeated studies it has been found that a scale factor of 2.03 gives a maximum deflection of 221.2 mm, identical to the drop test. It should also be noted that the deformation mode, illustrated in Figure 6.3, is not the same as for the dropped cylinder, and that maximum deformation occurs along the centerline.

The initial motivation for the cylinder drop test study was previous studies of the turbine foundation performed by Odfjell Oceanwind. They found unacceptable damage to the structure due to the OTG design pressures. This is not observed in this study, as the original pressure impulse only induces elastic vibrations of the structure. There are some differences in the modeling approaches, a significant difference being the stiffening of the structure: while the ring stiffener spacing in this study is 1 m, the design modeled by Odfjell Oceanwind had a stiffener spacing of 1.65 m. Such an increase in stiffener spacing will lead to a significant reduction in strength, and may explain the difference in the results.

It is difficult to determine a realistic impact velocity which corresponds to the peak pressure presented in DNV OTG-14. The drop tests reported in Kvålsvold, Faltinsen and Aarsnes [43] do not illustrate a uniform fit to Equation (4.1). In Chapter 5, it was found that the peak pressure on the 3 x 3 m^2 panel during the coupled drop test was 2.6 MPa. It would therefore be interesting to study the structural response of due to a drop with an impact velocity causing a peak pressure of 1.3 MPa on the panel, to see if this would give more comparable results to the response of the design pressure curve. Due to time restraints, this study has been left for further work.

The basis for the design pressures presented in DNV OTG-14 is considered unknown. It is specified in the technical guidance that the pressures have been *"calibrated against full scale observations of units subject to many years of service"* [7]. An earlier draft of the document is however found to allow design pressures well over 2 MPa without providing any explanation of why this value was lowered. The design pressures in the current version of the document are found to be much too low compared when compared to a simulated wave impact, both in regards to peak value and more importantly pressure impulse.

The effect of removing hydroelastic and -plastic effects was also studied, the results of which were presented in Figure 6.5. Compared to the fully coupled drop test, there was a reduction in maximum deflection of 28 mm and permanent deflection of 50.8 mm. The structural response history was similar in both cases, but larger elastic vibration, with a maximum vibration amplitude of about 28 mm, were present in the uncoupled analysis. In this case, the uncoupled analysis yields unconservative results. This contradicts expectations, as neglecting coupling effects is typically considered a conservative approach. When compared with the design pressure in DNV OTG-14, the uncoupled analysis however gives a much better approximation of the structural response of the cylinder.

The impulse of the rigid pressure load was found to be 110.8 kPa·s. This is very close to the pressure impulse on the same panel of the deformable drop test, which was found to be 110.5 kPa·s. This may give some explanation as to why the rigid pressure impulse gives a structural response in the same range as the coupled drop simulation.

The cylinder loaded with the pressure impulse from the coupled deformable simulation also illustrates a reduction in deformations. There are several effects which may contribute to this. The pressure impulse applied in this chapter is averaged over the panel, meaning local variations are smoothed. The oscillations in the pressure history in Figure 6.6 may be caused by local effects on the panel cancelling each other out, leading to a total lower impulse than what may be expected otherwise. Only pressures acting on the panel are also used in this recreation, while in the coupled analysis pressures are caused on the entire bottom surface of the cylinder. The increase in elastic vibrations may also be explained by the lack of added mass for the stationary cylinder, while these effects are present in the wet impact simulations. Interestigly, the reduction in structural response found in this thesis contradicts previous work by i.e. Rolland [1], who found an increase in structural response when applying the measured impulse to the undeformed structure.

Chapter 7

Discussion

There is a variable degree of accuracy between the numerical and experimental results. In Chapter 3, it was illustrated that the numerical model struggled to reproduce elastic recovery of the plate after maximum deflection. The accuracy of the results varied with the impact velocity, with the limiting cases yielding less accurate results. However, the overall accuracy of the numerical simulations was considered good. Some of the discrepancies observed may also be explained by the simplifications introduced to the model as well as material choice for the structure. As these factors are independent from the structural model of the cylinder, the numerical results in Chapter 3 validate the numerical settings of the fluid-structure interaction modeling.

An issue observed with the plate drop simulations, was the issue of leakage. While measures were implemented to remedy the problem, no useful solution was found. However, this issue was not observed in the cylinder drop test simulations, neither for the rigid nor the deformable cylinder. While the issue may have affected the accuracy of the results in Chapter 3, it is therefore not expected to affect the reliability of the cylinder models.

FSI coupling between air and the structure is not defined in neither the plate models nor the cylinder models. According to Greenhow and Yanbao [3], air effects are considered negligible during water impact of a cylinder, while they may play an important role for impacts with deadrise angle less than 3° such as the plate impact

modeled here. Especially in the plate impact model, is would be interesting to study these effects by also including coupling to the air. On the other hand, it would also be intersting to study if the vibrations of the rigid pressure curve may be explained by entrapped air by performing a simulation without the air present.

Chapter 6 illustrated the large discrepancy between the structural response to a drop simulation and DNV OTG-14 design pressures. While the drop test lead to significant plastic deformations, the design pressure only caused elastic vibrations. For the column geometry used in this thesis, the design pressures are therefore found to be insufficient. It should be noted that previous work by Skjeggedal [29] found good correspondence between drop simulations and design pressures for a semi-submersible platform column. The OTG also specifies that hydroelastic effects are not accounted for in the design pressures although these are considered significant. The results presented in this thesis illustrates these deficiencies.

The design pressures in DNV OTG-14 are specified to be used in ULS design considerations. In the ULS, it is required that the cylinder shall survive without permanent damange, which is satisfied by the response to the pressure impulse. This is however not satisfied in the drop simulation, where the impact velocity is calculated based on the ULS peak pressure and should therefore also be considered an ULS analysis. If the cylinder drop test was considered with regards to ALS, the initial condition of survivability is satisfied: although the structure is permanently deformed, no failures occur in the original model. The second stage of the ALS analysis would be a residual capacity analysis, which has been left for further work.

All drop simulations in this thesis has been performed with a structure with initial velocity entering still water. Another possible approach is to hold the structure still, while the initial velocity is applied to the water domain, more realistically modeling wave impact. Interestingly, Truong et. al. [2] found better accuracy in pressure history of a flat plate impact simulation with hitting water rather than dropping plate. While the dropping plate was found to overestimate the deformations, the hitting water underestimated deformations. It would therefore be interesting to study this alternative modeling approach in both the plate and cylinder impact simulations.

A documented flaw with the numerical modeling approach, is the inability to model ventilation. This has also been a problem documented in previous Master's theses, i.e. in Skjeggedal [29]. While Truong et. al. [2] illustrated the ability to model this phenomenon using ALE coupling in LS-DYNA, a reproduction of these results has not been attempted in the thesis work. This should however be studied further in order to improve the numerical modeling technique.

Non-reflective boundary conditions on the boundaries of the water domain were applied for the cylinder model and not for the flat plate drop simulations. While the plate drop simulations found good correspondence with experimental results without the non-reflective B.C.s, the rigid cylinder drop test corresponded better to theory when boundary conditions were applied. The convergence study of the plate drop simulations was however performed before the boundary conditions were applied, so better results may have been found with a new convergence study.

In the simulations presented in this thesis, strain rate effects have been neglected. Rolland [1] studied the effect of including strain rate effects in the flat drop test which in the experiment reached a maximum deformation of 23.41 mm. The differences between simulations including and excluding strain rate effects were in the range of 1 mm, with including strain rate effects yielding somewhat more accurate results. Slightly more accurate results may therefore be found when including these effects in the models presented in this thesis as well, but this has been left for further work.

Chapter 8

Conclusions

Numerical simulations of experimental drop tests using the ALE capabilities of LS-DYNA were carried out. The simulations provided good estimations of the structural response, both for flat plate impact and impact with deadrise angle 4°. While the numerical simulations slightly overestimated the maximum deformations of the flat plate, maximum deformations of the angled impact were somewhat underestimated. The good agreement in results illustrates that the chosen modeling approach is successful in describing the FSI during the slamming impact, despite the simplifications introduced.

Wave impact on a cylindrical floating wind turbine foundation column was studied trough numerical simulations of drop tests. Significant permanent deformations were found to the structure due to slamming impact with impact velocity 20 m/s. Limiting cases place maximum permanent deformations between 160 mm and 415 mm for a column with diameter 12 m and thickness 25 mm, with realistic deformations closer to the lower limit. The deformations and residual stresses after impact are expected to give a large reduction in capacity for the damaged structure. Results are verified by the good agreement between rigid cylinder impact pressure impulse from numerical simulations and analytical theory.

Column response due to the application of DNV OTG-14 pressure loads is found to significantly underestimate the deformations found during comparable coupled FSI drop simulations. The design pressures yield a severely unconservative re-

sponse for the structure, causing no permanent deformations. The OTG pressures are therefore found insufficient in describing the structural response due to slamming impact of the column analysed in this thesis, illustrating the need for further studies.

8.1 Further work

Further work should focus on improving the numerical modeling technique. Effects of entrapped air and strain rate hardening have both been neglected in the simulations in this thesis. Further modeling should focus on implementing these effects. Furthermore, it should be established whether air effects are the reason negative pressures are not reproducible using the modeling technique applied here, and if not, why this is the case. The possibility of replacing the simulated drop tests with impacting water domains should also be studied, as this has proven to yield more accurate results in some previous works. Finally, an even more accurate modeling approach is possible by coupling a structural solver with a CFD solver for more advanced modeling of the fluid flows, which should be investigated.

For a full assessment of the slamming wave impact on the cylindrical column, further analysis should be performed. Residual capacity analyses should be performed, identifying the strength of the column in damaged condition after impact.

Finally, this thesis has illustrated the necessity of further studies of the DNV OTG-14 pressure curves. While previous works have found the pressures to give good estimations of slamming loading, they are found inaccurate for application on the cylindrical column studied in this thesis. Further studies should therefore be performed to identify parameters which may affect these results. Possible alternative approaches should also be investigated.

Bibliography

[1] Rolland LA. Fluid structure interaction analysis of abnormal wave slamming events. Master's Thesis, Norwegian University of Science and Technology 2018.

[2] Truong DD, Jang BS, Ju HB, Han SW. Prediction of slamming pressure considering fluid-structure interaction. part i: numerical simulations. *Ships and Offshore Structures* 2022; **17**(1):7–28.

[3] Greenhow M, Yanbao L. Added masses for circular cylinders near or penetrating fluid boundaries—review, extension and application to water-entry,-exit and slamming. *Ocean engineering* 1987; **14**(4):325–348.

[4] DNV. *DNV-RP-C204 Design against accidental loads* 2010.

[5] Moan T. *Finite Element Modelling and Analysis of Marine Structures*. NTNU Dept. Marine Technology, 2003.

[6] Holen ML. Debunking some myths about offshore wind's role in the energy transition. URL https://knowledge.odfjell-oceanwind.com/debunking-some-myths-about-offshore-winds-role-in-the-energy-transi

[7] DNV. *DNV-OTG-14 Horizontal wave impact loads for column stabilised units* 2019.

[8] Petrolueomstilsynet. Granskingsrapport etter hendelse med fatalt utfall på coslinnovator 30. desember 2015. 2016.

[9] von Karman T. The impact on seaplane floats during landing. *Technical Report*, NAtional Advisory Comittee for Aeronautics 1929.

[10] Wagner H. Über stoß- und gleitvorgänge an der oberfläche von flüssigkeiten. *Journal of Applied Mathematics and Mechanics* 1932; **12**(4):103–215.

[11] Zhao R, Faltinsen O. Water entry of two-dimensional bodies. *Journal of fluid mechanics* 1993; **246**:593–612.

[12] Cointe R, Armand JL. Hydrodynamic impact analysis of a cylinder. *Journal of Offshore Mechanics and Arctic Engineering* 1987; **109**(3):237–243.

[13] Korobkin A. Analytical models of water impact. *European Journal of Applied Mathematics* 2004; **15**(6):821–838.

[14] Aarsnes JV. An experimental investigation of the effect of structural elasticity on slamming loads and structural response. *Technical Report*, MARINTEK A/S 1994.

[15] Faltinsen OM, Kvålsvold J, Aarsnes JV. Wave impact on a horizontal elastic plate. *Journal of Marine Science and Technology* 1997; **2**(2):87–100.

[16] Kvalsvold J, Faltinsen OM. Hydroelastic modeling of wet deck slamming on multihull vessels. *Journal of ship research* 1995; **39**(03):225–239.

[17] Faltinsen OM. The effect of hydroelasticity on ship slamming. *Philosophical Transactions of the Royal Society of London. Series A: Mathematical, Physical and Engineering Sciences* 1997; **355**(1724):575–591.

[18] Mori K. Response of the bottom plate of high speed crafts under impulsive water pressure. *Journal of the Society of Naval Architects of Japan* 1977; **1977**(142):297–305.

[19] Abrahamsen BC, Alsos HS, Aune V, Fagerholt E, Faltinsen OM, Hellan Ø. Hydroplastic response of a square plate due to impact on calm water. *Physics of Fluids* 2020; **32**(8):082 103.

[20] Jones N. A theoretical study of the dynamic plastic behavior of beams and plates with finite-deflections. *International Journal of Solids and Structures* 1971; **7**(8):1007–1029.

[21] Yu Z, Amdahl J, Greco M, Xu H. Hydro-plastic response of beams and stiffened panels subjected to extreme water slamming at small impact angles, part i: An analytical solution. *Marine Structures* 2019; **65**:53–74.

[22] Yu Z, Amdahl J, Greco M, Xu H. Hydro-plastic response of beams and stiffened panels subjected to extreme water slamming at small impact angles, part ii: Numerical verification and analysis. *Marine Structures* 2019; **65**:114–133.

[23] Jones N. Slamming damage. *Journal of Ship Research* 1973; **17**(02):80–86.

[24] Cheon JS, Jang BS, Yim KH, Lee HD, Koo BY, Ju H. A study on slamming pressure on a flat stiffened plate considering fluid–structure interaction. *Journal of Marine Science and Technology* 2016; **21**(2):309–324.

[25] Stenius I, Rosén A, Kuttenkeuler J. Hydroelastic interaction in panel-water impacts of high-speed craft. *Ocean Engineering* 2011; **38**(2-3):371–381.

[26] Truong DD, Jang BS, Janson CE, Ringsberg JW, Yamada Y, Takamoto K, Kawamura Y, Ju HB. Benchmark study on slamming response of flat-stiffened plates considering fluid-structure interaction. *Marine Structures* 2021; **79**:103 040.

[27] Muren MM. Response calculations of semi-submersible column exposed to slamming loads. Master's Thesis, Norwegian University of Science and Technology 2016.

[28] Anglade C. Load and response calculation from breaking wave impacts on columns of semisubmersible platforms. Master's Thesis, Norwegian University of Science and Technology 2017.

[29] Skjeggedal E. Wave-in-deck forces and response of semi-submersibles. Master's Thesis, Norwegian University of Science and Technology 2017.

[30] Faltinsen OM. Hydroelastic slamming. *Journal of Marine Science and Technology* 2000; **5**(2):49–65.

[31] Cao A. Fsi analysis of abnormal wave slamming events. Master's Thesis, Norwegian University of Science and Technology 2020.

[32] Kingell BC. Fluid structure interaction analysis of abnormal wave slamming events. Master's Thesis, Norwegian University of Science and Technology 2021.

[33] DNV. *DNV-OTG-13 Prediction of air gap for column stabilised units* 2019.

[34] Faltinsen OM. *Hydrodynamics of high-speed marine vehicles*. Cambridge university press, 2005.

[35] DNV. *DNV-RP-C205 Environmental Conditions and Environmental Loads* 2014.

[36] Moan T. *Design of Marine Structures*, vol. 1. Department of Marine Structures, NTNU, 2000. Part I.

[37] DYNAmore GmbH. Dynamore exress: Beyond fea: Arbitary lagrangean-eulerian (ale) method May 2022. URL https://www.youtube.com/watch?v=wXXORbcRPjI&t=2130s&ab_channel=DYNAmoreGmbH, speaker Maik Schenke.

[38] Hallquist JO. *LS-DYNA Theory Manual*. LSTC 2006.

[39] Hopperstad OS, Børvk T. Lecture notes impact mechanics - part 1: Modelling of plasticity and failure with explicit finite element methods Fall 2021.

[40] Livermore Software Technology Corporation. *LS-DYNA Keyword User's Manual Vol. I,II* 2017.

[41] Barrett T. Dnv awards odfjell oceanwind aip for new deepsea semi™ floating offshore wind foundation. URL https://www.dnv.com/news/dnv-awards-odfjell-oceanwind-aip-for-new-deepsea-semi-floating-offs

[42] Storheim M. Structural response in ship-platform and ship-ice collisions. PhD Thesis, Norwegian University of Science and Technology 2016. Faculty of Natural Sciences and Technology, Department of Marine Technology.

[43] Kvalsvold J, Faltinsen OM, Aarsnes JV. Effect of structural elasticity on slamming against wetdecks of multihull vessels. *Journal of Ship and Ocean Technology* 1997; **1**(1):1–14.

[44] Dassault Systems. The abaqus products 2019. URL https://help.3ds.com/2019/english/dssimulia_established/SIMACAEGSARefMap/simagsa-c-intabamod.htm?contextscope=all&id=a29e426680804c2cb415d333e06f92bb, (accessed: 01.07.2022).

[45] Dassault Systems. Equation of state 2019. URL https://help.3ds.com/2019/english/dssimulia_established/SIMACAEMATRefMap/simamat-c-eos.htm?contextscope=all&id=5bcdde5f885a46f18241b17132fc5924, (accessed: 03.02.2022).

[46] Abaqus Acumen. Abaqus coupled eulerian lagrangian (cel) modelling tutorial: Example- can drop test 2017. URL https://www.youtube.com/watch?v=EJ1kVE8KEHY&ab_channel=AbaqusAcumen, (accessed: 09.02.2022).

[47] Dassault Systems. About mechanical contact properties 2019. URL https://help.3ds.com/2019/english/dssimulia_established/SIMACAEITNRefMap/simaitn-c-contactmechanical.htm?contextscope=all, (accessed: 25.02.2022).

Appendices

Appendix A

Calculation of slamming pressures

Greenhow and Yanbao's [3] solution of Wagner's slamming theory for a rigid cylinder included an infinite series, as previously given in Equations (2.7) and (2.8). MATLAB has been used to calculate the infinite series, recreating Figure 11 from Greenhow and Yanbao in Figure 2.1. The relations have been used further in the numerical calculation of the pressure distributions illustrated in Section 4.2.

MATLAB allows for the definition of symbolic variables and functions which behave like variables and functions in calculus. Firstly, the summation index m and the variable c/R are defined as symbolic variables using the *syms* function. Defining Equations (2.7) and (2.8) as functions of the symbolic variables, these become symbolic functions. The MATLAB function *symsum* calculates the sum of the symbolic series for symbolic index *m* from 0 to infinity. The series then become functions only of the symbolic variable c/R. To allow for use of the calculated series, the symbolic functions must be evaluated for each c/R. This is performed using the MATLAB functions *subs* and *double*. The relations illustrated in Figure 2.1 are then given numerically, and are used further in pressure calculations according to Section 2.1. The full code for the calculations is given below.

A.1 MATLAB code

```
% Pressure time history for rigid cylinder. Pressures calculated from
% Wagner theory, and wetted surface predicted from Equation (39) and (40)
% in Greenhow and Yanbao (1987).
clear
clc
close all

R = 6; % [m]
V = 20; % [m/s]
rho = 1025; % [kg/m^3]

% --- Calculating the series ---
syms x m

E39 = symsum( factorial(2*m+1)*factorial(2*m-1)/(2^(4*m)*factorial(m)^2*...
    factorial(m+1)*factorial(m-1))*x^(2*m+1), m, 0, Inf);

E40 = symsum( factorial(2*m+1)*factorial(2*m-1)/(2^(4*m)*factorial(m)^2*...
    factorial(m+1)*factorial(m-1)*(2*m+2))*x^(2*m+2), m, 0, Inf);

c = 0:0.001:1; % [-]
u = zeros(1, length(c)); % [-]
del = u; % [-]

for i = 1:length(c)-1
    x = c(i);
    A = subs(E39);
    u(i) = double(A);    % Evaluating Eq. (39)
    B = subs(E40);
    del(i) = double(B);  % Evaluating Eq. (40)
end
x = c(end);
B = subs(E40);
del(end) = double(B);

figure(1)
plot(c(1:end-1), u(1:end-1), c, del, 'linewidth', 1.3)
legend('\mu(c)', '\delta=Vt/R', 'Location', 'northwest')
set(gcf,'position',[100,100,300,450])
xlabel('c/R')
```

```
xlim([0 1.05])
grid on

% --- Calculating the pressures ---
c = c*R;
t = del*R/V;
dc = V./u;

x=0:0.01:R;
p = zeros(length(t)-2, length(x));

for i=2:length(t)-1
    j=1;
    while (j<=length(x) && x(j)<=c(i))
        p(i-1,j) = rho*V *c(i)*dc(i) / sqrt(c(i)^2-x(j)^2);
        j=j+1;
    end
end

figure(2)
hold on
for i=1:size(p,1)
    plot(x, p(i,:)/(10^6), 'linewidth', 1.2)
end
xlabel('x-coordinate (m)')
ylabel('Presure (MPa)')
ylim([0 4*10^2])

figure(3)
plot([-0.005 t(1:end-1)], [0; 0; p(:,1)]/(10^6), 'linewidth', 1.2)
plot([-0.005 t(1:end-1)], [0; 0; p(:,101)]/(10^6), 'linewidth', 1.2)
xlabel('Time (s)')
xlim([-0.005 0.12])
ylabel('Pressure (MPa)')
ylim([0 8])

% Calculating pressure impulse
imp = trapz(t(1:end-1), [0; p(:,1)]);
fprintf('Impulse at location x=%i is %.3f MPa*s.\n', x(1), imp/10^6)
imp = trapz(t(1:end-1), [0; p(:,101)]);
fprintf('Impulse at location x=%i is %.3f MPa*s.\n', x(101), imp/10^6)
```

```
%read_dbfsi
%read_dbsensor
```

Appendix B

FSI modeling in Abaqus

An initial study was performed into the FSI capabilities of the finite element solver Abaqus. Abaqus is a general-purpose solver from SIMULIA with standard packages for static, dynamimc, thermal, electrical and electromagnetic problems. Add-ons are also available for modeling of waves and wind for offshore applications and more [44]. The solver allows for FSI coupling through a Coupled Eulerian-Lagrandian contact formulation. Abaqus/CAE 2019 has been used for modeling and running simulations in this thesis.

As Abaqus was used in the initial stages of modeling, a simple model of the plate drop was attempted. Air was not modeled, but instead replaced by a void. Coarse meshes were used, as no convergence of mesh was studied as of yet. The material models used in the Abaqus model are also not as accurate representations as in the final version of the LS-DYNA model presented in Chapter 3.

B.1 Lagrangian structural model

In Abaqus modeling, a material should firstly be defined. Simple elastic material models were implemented for both aluminium and steel. Density, Young's modulus and Poisson's ratio were defined for both materials, as in the material descriptions in the LS-DYNA model. The thickness of both plates was assumed to be 0.6 mm also in this model.

The geometry of both plates were modeled as described in Section 3.2, using a 3D deformable definition. For the steel plate, a reference point was created as this is necessary for the rigid modeling. The plates were meshed using linear 4-noded shell elements with reduced integration, using structured mesh control to gain a regular mesh. In order to make the steel plate rigid, a rigid body constraint was defined using the reference point. The two plates were connected by a tie constraint, defining the rigid steel plate as the master surface and the aluminuim plate as the slave. The initial impact velocity of both plates were created as boundary conditions, applied separately to the two plates.

B.2 Eulerian fluid model

A 3D Eulerian solid box was created for the Eulerian domain. As previously mentioned, the Eulerian domain in the model included water and void, so only one material definition was necessary. The material properties of water were defined as listed in Table B.1. For fluids, the material definition should also contain an EOS. While the Gruneisen EOS is commonly used for water modeling in LS-DYNA, only a simplified version of this, called the Us-Up EOS, is available as a default in Abaqus. The EOS is given in Equation (B.1) [45], but may be rewritten as Equation (B.2) to illustrate the connection to the Gruneisen EOS in Equation (2.28).

Table B.1: Material properties of the water in Abaqus model.

Property	Value
Density [kg/m^3]	1000
Viscosity [mPa]	1.0016
c [m/s]	1450
s [-]	0.0
γ_0 [-]	0.0
E_m [J/kg]	0.0

$$p = \frac{\rho_0 c^2 \eta}{(1 - s\eta)^2}\left(1 - \frac{\gamma_0 \eta}{2}\right) + \gamma_0 \rho_0 E_m \tag{B.1}$$

$$p = \frac{\rho_0 c^2 \mu\left(1 + \left(1 - \frac{\gamma_0}{2}\right)\mu\right)}{(1 - (s-1)\mu)^2} + \gamma_0 E \tag{B.2}$$

ρ_0 is the initial density of the material, E_m is the internal energy per mass and E is the internal energy per volume. η and μ share similar definitions and depend on the relation between current and initial density: $\eta = 1 - \frac{\rho_0}{\rho}$ and $\mu = \frac{\rho}{\rho_0} - 1$. c, s, γ_0 and E_m are material parameters which must be defined. Density, viscosity and speed of sound in the material c, are all taken as default values for water, while the rest of the EOS parameters are left equal to zero, as recommended by Abaqus Acumen [46]. A solid Eulerian section definition with water was defined for the entire Eulerian domain, but will in principle only affect the region of the domain where water filling is defined.

In addition to the Eulerian domain, the fluid model also included two more parts: a rigid box to contain the domain, as well as a dummy box which was used for filling the correct section of the Eulerian domain with water.

Meshing of the Eulerian domain was performed using structural control for a regular mesh. Eulerian solid elements with an approximate size of 50 mm were used. Water filling of the correct area was performed using the volume fraction tool. The Eulerian domain was firstly chosen as the intended target, thereafter choosing the dummy box located in the nether section of the domain as the area which shall be filled. This creates a discrete field, which when defined as a predefined field creates material assignment to the water part of the Eulerian domain. The dummy box is thereafter removed from the assembly of the model.

B.3 Coupling

Coupling between the Lagrangian structure and the Eulerian fluid is defined through a contact definition. General contact is defined for all surfaces, with interaction properties defined for both tangential and normal behaviour. Based on recommendations from Abaqus Acumen [46], penalty coupling is defined for the tangential behaviour and hard contact is defined for the normal behaviour. Hard contact in Abaqus is defined so that pressures are transmitted when nodes of the master and slave surface are in contact, and no penetration is allowed to occur [47]. This may be considered an extreme version of the penalty coupling.

B.4 Results

The midpoint deflections of the plate due to a simulated drop from 778 mm are illustrated in Figure B.1. The plate experiences permanent deformations of about 6.0 mm, with oscillations with amplitude of about 10 mm. The water upwell due to the impact is illustrated in Figure B.2.

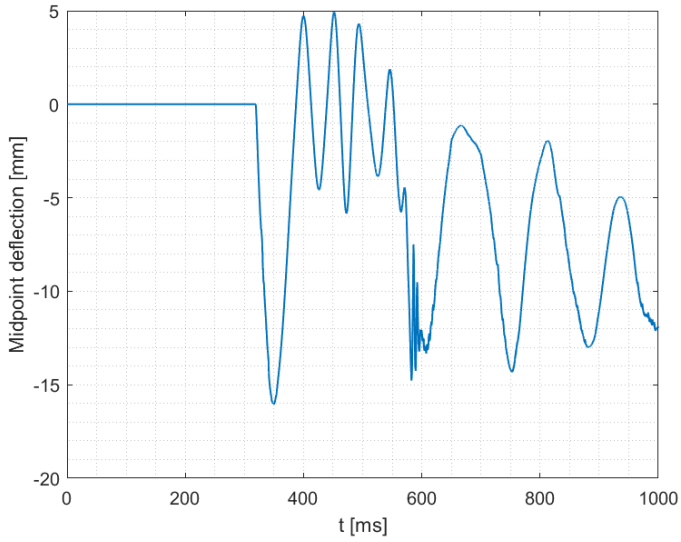

Figure B.1: Midpoint deflection of plate, drop height 778 mm.

Due to the bad accuracy of the results from the initial modeling, Abaqus was abandoned for LS-DYNA, as this has previously been verified for FSI modeling. It should be noted that the benchmark FSI modeling study by Truong et. al. [26] included Abaqus in the study, but only in co-simulation with CFD software. It would nevertheless be interesting to study if the results could be improved using Abaqus, but this has not been studied due to time constraints.

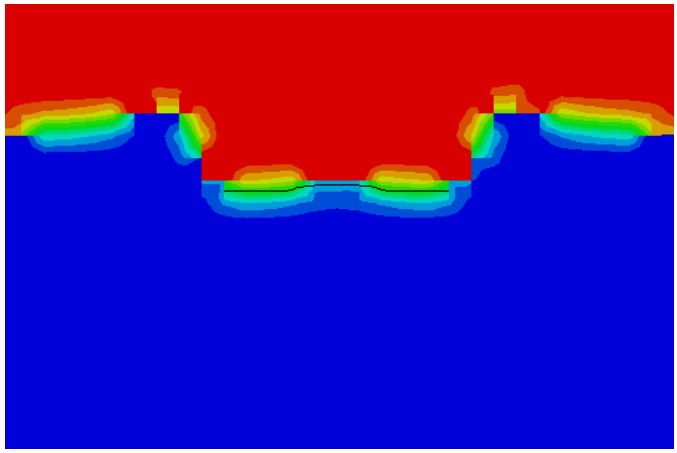

Figure B.2: Fluid upwell due to plate impact.

Appendix C

Calculation of DNV OTG-14 pressure curve

As previously explained, DNV OTG-14 [7] gives ULS design pressures for column-stabilised offshore units to be applied to 3 x 3 m^2 and 6 x 6 m^2 panels. The maximum peak pressure value to be applied to a 3 x 3 m^2 panel is 1.3 MPa. The pressure curve should also include pressure levels which should be sustained for 9 ms, 50 ms and 100 ms. The sustained pressures relative to the peak pressure are given graphically in Figure 3 in the OTG.

Figure 3 from the OTG is reproduced in Figure C.1 included markings for the relevant load levels. Given a peak pressure of 1.3 MPa, a pressure ratio of 0.58 should be sustained for 9 ms, a ratio of 0.20 for 50 ms and a ratio of 0.13 for 100 ms. The corresponding pressures are reported in Table C.1. No recommondations are given with regards to the fall time to zero pressure or total duration of the pressure history, so this has been set to 150 ms. The resulting pressure history is presented in Figure C.2.

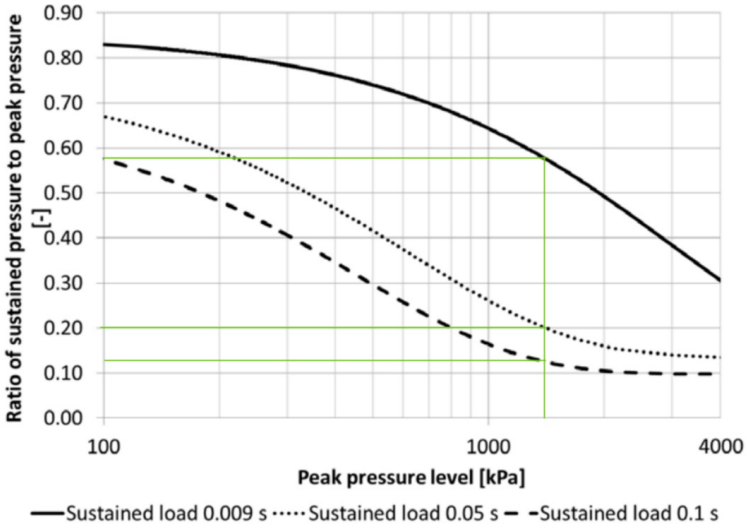

Figure C.1: Sustained pressure ratios, based on peak pressure of 1.3 MPa. Original figure reproduced from DNV OTG 14 [7].

Table C.1: Data for the OTG 14 design pressure history.

Duration [ms]	**Pressure** [kPa]
Peak	1300
9	754
50	260
100	169

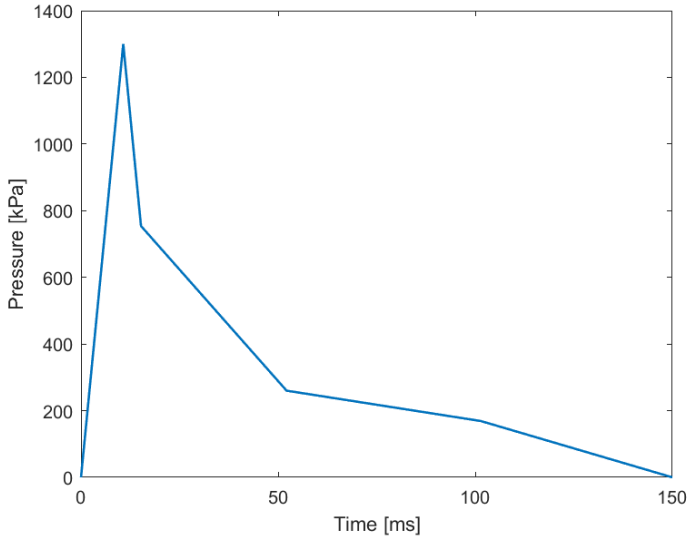

Figure C.2: Worst case pressure curve, produced based on DNV OTG 14 [7].

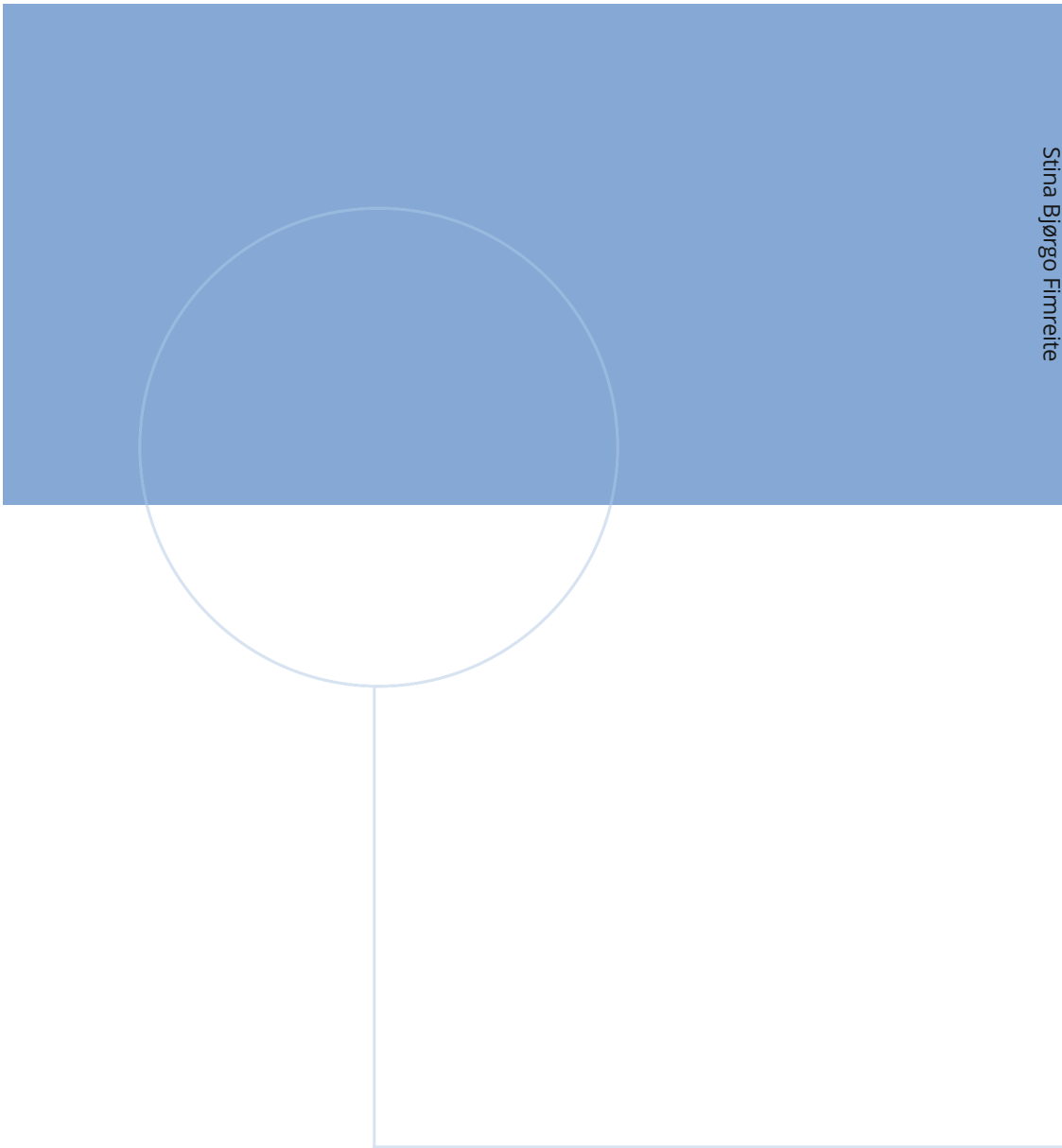

Stina Bjørgo Fimreite

NTNU
Norwegian University of
Science and Technology